



HAL
open science

Unraveling the link between magma and deformation during slow seafloor spreading

Yanghui Zhao, Weiwei Ding, Gianreto Manatschal, Xiaodong Wei, Hanghang Ding, Zhengyi Tong, Jingyan Zhao

► **To cite this version:**

Yanghui Zhao, Weiwei Ding, Gianreto Manatschal, Xiaodong Wei, Hanghang Ding, et al.. Unraveling the link between magma and deformation during slow seafloor spreading. *Tectonophysics*, 2024, 889, 10.1016/j.tecto.2024.230473 . insu-04725702

HAL Id: insu-04725702

<https://insu.hal.science/insu-04725702v1>

Submitted on 8 Oct 2024

HAL is a multi-disciplinary open access archive for the deposit and dissemination of scientific research documents, whether they are published or not. The documents may come from teaching and research institutions in France or abroad, or from public or private research centers.

L'archive ouverte pluridisciplinaire **HAL**, est destinée au dépôt et à la diffusion de documents scientifiques de niveau recherche, publiés ou non, émanant des établissements d'enseignement et de recherche français ou étrangers, des laboratoires publics ou privés.



Distributed under a Creative Commons Attribution - NonCommercial 4.0 International License



Unraveling the link between magma and deformation during slow seafloor spreading

Yanghui Zhao^{a,**}, Weiwei Ding^{a,b,*}, Gianreto Manatschal^c, Xiaodong Wei^a, Hanghang Ding^d, Zhengyi Tong^d, Jingyan Zhao^a

^a Key Laboratory of Submarine Geosciences, Second Institute of Oceanography, Ministry of Natural Resources, Hangzhou 310012, China

^b School of Oceanography, Shanghai Jiao Tong University, Shanghai 200030, China

^c Université de Strasbourg, CNRS, ITES UMR 7063, Strasbourg F-67084, France

^d School of Earth Sciences, Zhejiang University, Hangzhou 310027, China

ARTICLE INFO

Keywords:

Slow mid-ocean ridges
Life cycle of oceanic core complex
Fault pattern variation
Tectono-magmatic interaction

ABSTRACT

Detachment faulting related to oceanic core complexes (OCCs) has been suggested to be a manifestation of slow seafloor spreading. Although numerical models suggest OCCs form under low magma supply, the specific interaction between magmatism and tectonic faulting remains elusive. This paper examines seismic observations detailing the spatiotemporal interactions between magmatism, high-angle faulting, and detachment faulting at a slow-spreading mid-ocean ridge in the West Philippine Basin. We identified a magma-rich spreading phase, indicated by a magmatic top basement and oceanic crust with shallow-penetrating high-angle normal faults. An axial valley reveals an along-strike transition from magmatically-dominated to highly tectonized oceanic crust over a distance of 70 km. Two older OCCs with concave-down fault geometries and a younger OCC with steep-dipping faulting suggest sequential detachments with the same polarity. Our findings suggest: (1) slow seafloor spreading alternates between high-angle faulting with a relatively high magma supply and detachment faulting with a limited magma supply; (2) sequential development of younger detachments in the footwall of its predecessor leads to an asymmetric split in the newly accreted crust; and (3) the life cycle of OCC ends with high-angle faults that overprint the detachment and act as magma pathways, sealing the OCC. Our study captures the dynamic interaction between high-angle and detachment faults and their concurrent and subsequent relationship to magmatic systems. This reveals that strain distribution along strike is critical to OCC formation, thus enriching our understanding beyond conventional considerations such as spreading rates and melt budgets at mid-ocean ridges.

1. Introduction

Spreading rate is often considered a key factor in controlling crustal accretion at mid-ocean ridges (MORs) (e.g., Bell and Buck, 1992; Chen and Morgan, 1990). Oceanic core complexes (OCCs) are prominent at the Mid-Atlantic Ridge (MAR) with spreading rates of approximately 14–32 mm/yr (e.g., Cann et al., 1997; Zhang et al., 2022a) and at the Southwest Indian Ridge (SWIR), where rates fall below 14 mm/yr (e.g., Cannat et al., 2006). The emergence of OCCs in areas with slow spreading rates highlights the role of detachment faults in plate splitting when tectonic extension prevails under conditions of low melt supply (e.g., Lin et al., 1990; Tucholke et al., 2008). Numerical models further

reveal that when magma supply falls below a critical threshold, it can initiate large-offset detachment faults; these faults are responsible for exhumation of oceanic lower crust (gabbros) and mantle to the seafloor, highlighting the interplay between magma availability and fault dynamics (Behn and Ito, 2008; Buck et al., 2005; Liu and Buck, 2020; Olive et al., 2010; Tucholke et al., 2008).

Building on these insights, kinematic models have been developed to explain the processes occurring in slow and ultraslow spreading MORs (Fig. 1). For the slow-spreading MAR, a model proposing long-lived detachment faults has been introduced (MacLeod et al., 2009). This model suggests an OCC with a detachment fault that developed through a runaway weakening of a high-angle normal fault, subsequently being

* Corresponding author at: Key Laboratory of Submarine Geosciences, Second Institute of Oceanography, Ministry of Natural Resources, Hangzhou 310012, China.

** Corresponding author.

E-mail addresses: zhaoyh@sio.org.cn (Y. Zhao), wwding@sio.org.cn (W. Ding).

cut by dikes, and eventually terminating when sufficient melt is delivered to the surface of the footwall (Figs. 1A-1D). For the ultraslow spreading SWIR, the dynamic ‘flip-flop’ model addresses successive and short-lived detachment faults (Figs. 1E-1H). According to this model, the alternating polarity of detachment faulting controls mantle exhumation and terminates when extrusion occurs in magma-starved conditions (Reston and McDermott, 2011; Sauter et al., 2013). These models imply a coupled relationship between magmatism and detachment faulting, with magmatism occurring only when previously active detachment faults are exposed on the seafloor.

Field observations from the Alpine Tethys, however, suggest that magmatism may persist during active detachment faulting (MacLeod et al., 2002; Manatschal et al., 2011; Coltat et al., 2020). This is particularly well documented at the Chenaillet Ophiolite, where high-angle normal faults, offsetting previous exhumed detachment surfaces, are serving as pathways for magmas (Manatschal et al., 2011). Furthermore, various petrological and numerical studies suggest that magmatism can efficiently localize the strain at the root of detachment faults during slow seafloor spreading (Cannat et al., 1991; Hansen et al., 2013; Schroeder and John, 2004). These studies propose that magmatism can indeed occur simultaneously with the formation of detachment faults. However, detailed insights into how magma supply triggers such faults and interacts with crustal accretion are yet rare. Moreover, the interaction between magmatic activity and tectonic faulting is crucial for controlling or modifying the thermal state and rheology of divergent plate boundaries at MORs (Cannat et al., 2019). Unraveling the link between magma and deformation, beside indirect insights into rheology, is feasible through high-quality seismic reflection sections.

Here, we present new observations from multichannel seismic (MCS) reflection profiles A-A’ and B-B’, which provide detailed imaging of the crustal structures of a slow-spreading MOR in the eastern West Philippine Basin (WPB) (Fig. 2). The MOR of the WPB, also known as the

Central Basin Fault (CBF, e.g., Deschamps et al., 2002), exhibits a significant change in orientation from E-W in its eastern segment to NW-SE in its western segment (Fig. 2A), indicating a significant shift in extensional direction from N-S to NE-SW (e.g., Deschamps et al., 2002). Profile A-A’ documents both N-S and NE-SW rift valleys, extending 130 km from the southwest ridge flank to the northern shoulder and running obliquely to the CBF (Fig. 2B). Profile B-B’ extends from NW to SE at the eastern edge of the N-S rift valley (Fig. 2A). The intersection of Profile A-A’ with the CBF at a 30° angle allows for the simultaneous examination of oceanic crustal structures. This setup enables the observation of structures extending 65 km across the MOR and 112 km along strike, thereby effectively capturing the crustal configuration. Meanwhile, Profile B-B’, which runs orthogonally to the mid-ocean ridge zone, i.e. the CBF, provides additional validation of the structures at the eastern end of the CBF. Consequently, these profiles allow us to assess both the spatial changes in the oceanic crustal structure subjected to varying magma supply and the interaction between magmatism and tectonic faulting during slow spreading at the MOR.

2. Geological setting

The WPB exhibits water depths ranging from 3 to 6 km, with a general shallowing trend from west to east (Deschamps et al., 2002) (Fig. 2A). The basin floor is covered predominantly by abyssal, <300 m thick, abyssal deposits (Zhang et al., 2022b). Our study focuses on the eastern MOR of the WPB, located between 132° E and 133.5° E longitude and 14.5° N and 147° N latitude (Fig. 2B). This eastern MOR of the WPB exemplifies a typical slow-spreading MOR system, characterized by a deep axial valley bounded by ridge shoulders with a 500-m relief. Notably, the axial valley displays pronounced segmentation, reflecting complex spreading processes in the WPB (Deschamps et al., 2002), which can be traced through three key phases (Fig. 3).

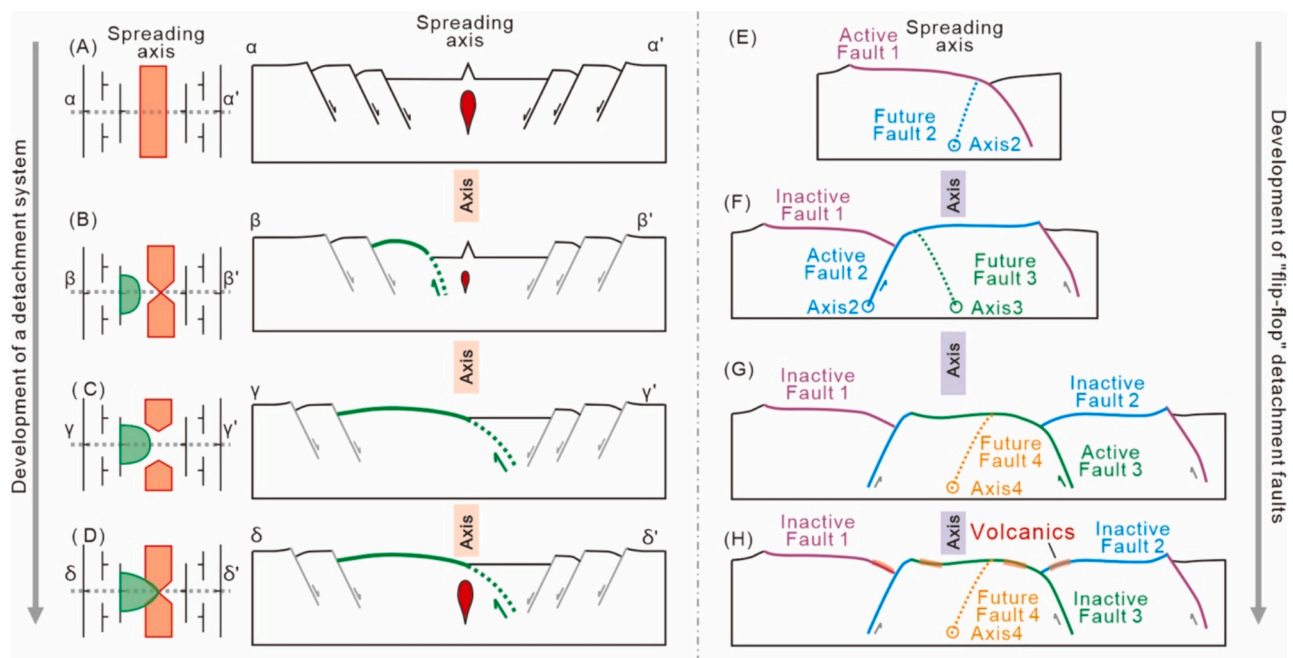


Fig. 1. Kinematic models for the formation of new oceanic crust at slow and ultraslow spreading mid-ocean ridges (MORs). (A-D) Evolution of a detachment fault system and the associated life cycle of an oceanic core complex (OCC), after MacLeod et al. (2009). The left column presents a map view of observed seafloor geology, with the volcanic zone in red, the emerged detachment fault in green, and the other high-angle normal faults in black. The right column provides vertical cross-sections across the spreading axis. (E-H) ‘Flip-flop’ model showing mantle exhumation on successive detachment faults (Reston and McDermott, 2011; Sauter et al., 2013). Following Reston (2018), we use ‘rift axis’ (marked by circles) to denote the divergence axis at fault initiation depth, distinct from the ‘spreading axis’ (colored by transparent bars) at the surface. These models highlight the close relationship between fault patterns and melt supply, suggesting magmatism occurs when inactive detachment faults are exposed on the seafloor. However, this is contradicted by observations of basal emplacement over previously exhumed detachment surfaces in the Chenaillet Ophiolite (Manatschal et al., 2011) and seismic data from this study, which imply that magmatism can coincide with detachment faulting. (For interpretation of the references to colour in this figure legend, the reader is referred to the web version of this article.)

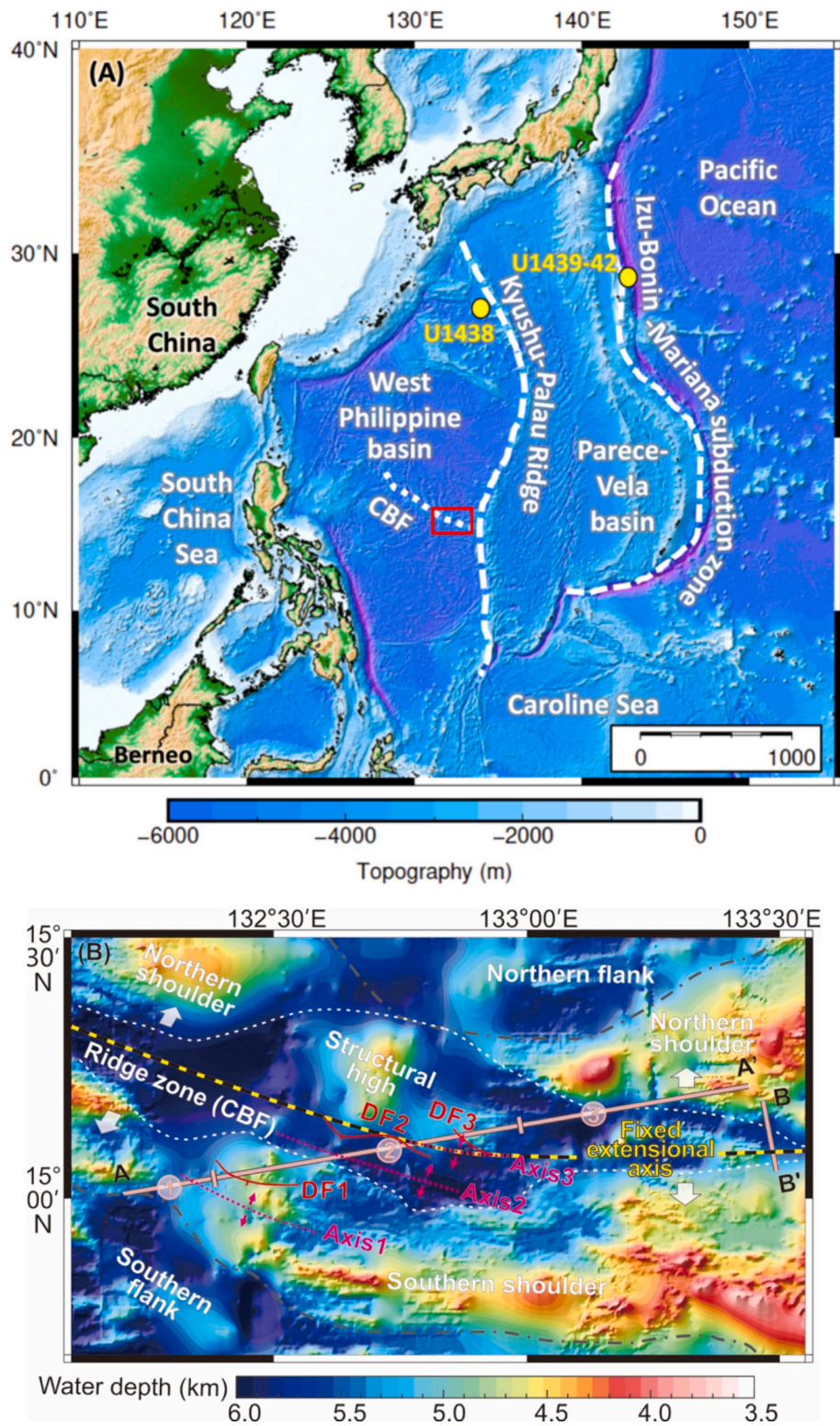


Fig. 2. (A) Shaded view of the satellite-derived bathymetry of the Philippine Sea Plate and major seafloor features of the West Philippine Basin, drawing on data from [Tozer et al. \(2019\)](#). Red box identifies the location of (B). Yellow dots indicate the locations of IODP expeditions 351 (U1438) and 352 (U1439–42) drill sites ([Arculus et al., 2019](#)). (B) Zoom-in of the central basin fault (CBF) of the eastern WPB and the locations of MCS reflection profiles A-A' and B-B'. Profile A-A' extends SW-NE oblique to the CBF, while profile B-B' extends NW-SE at the eastern extremity of the valley. The CBF divides into N-S and NE-SW rift valleys due to extensional reorientation ([Deschamps et al., 2002](#)). These perpendicular profiles demonstrate spatial and temporal variations of the slow-spreading MOR. A single fixed extensional (spreading) axis serves as the extension point, with surface rift axes 1, 2, and 3 resulting from detachment faults propagating upward and outward from this fixed point. (For interpretation of the references to colour in this figure legend, the reader is referred to the web version of this article.)

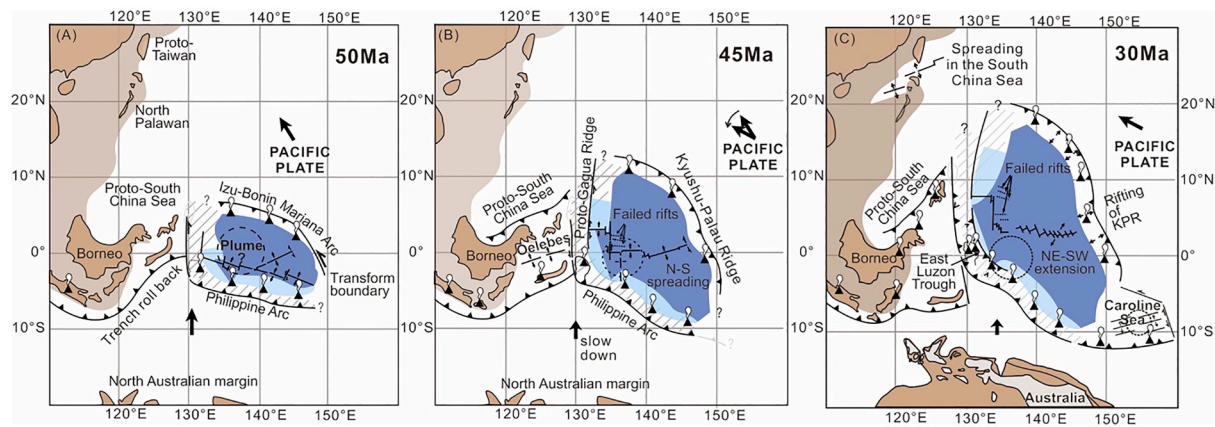


Fig. 3. Evolution model of the West Philippine Basin at 50 Ma (A), 45 Ma (B), and 30 Ma (C), following Deschamps and Lallemand (2002). (A) At 50 Ma, the seafloor was spreading in the N10W direction at a moderate rate (half-rate of 44 mm/a). (B) Around 45 Ma, a major plate reorganization extended from Southeast Asia through the western Pacific to Australia (e.g., Hall, 2002). In the WPB, the spreading rate decreased to a slow rate of 18 mm/a. (C) Around 33–30 Ma, a regional extension likely caused the latest reorientation from N-S to NE-SW (Deschamps et al., 2002).

(1) Initial spreading phase.

The onset of seafloor spreading in the WPB is estimated to have occurred around 60 Ma (Hilde and Lee, 1984), 55 Ma (Deschamps and Lallemand, 2002; Hall, 2012), 52–51 Ma (Ishizuka et al., 2013), or 50 Ma (Arculus et al., 2019). Before 45 Ma, the seafloor spreading direction was N10W at a moderate half-rate of 44 mm/a (Fig. 3A).

(2) Slow spreading phase.

Around 45 Ma, significant plate reorganization occurred from Southeast Asia through the western Pacific to Australia. This included a notable slowdown of subduction along the Philippine Arc (Ding et al., 2023; Hall, 2002) (Fig. 3B). Consequently, the driving force for WPB seafloor spreading weakened, reducing the half-rate to 18 mm/a while maintaining a N-S direction (Deschamps et al., 2002). This slow seafloor spreading stage is suggested to have ceased between 36 Ma (Chron17; Loudon, 1976; Mrozowski et al., 1982) and 33 Ma (Chron13; Hilde and Lee, 1984; Taylor and Goodliffe, 2004).

(3) Reorientation phase.

Between approximately 33 and 30 Ma, a significant reorientation of extensional directions from N-S to NE-SW occurred (Fig. 3C). This is evidenced by NW-SE-oriented fabrics intersecting pre-existing E-W fabrics (Deschamps et al., 2002). Although the precise timing of this reorientation remains uncertain, it is proposed to have occurred between 33 and 26 Ma, assuming that the basalts forming the ridge walls originated during this NE-SW oriented extension (Fujioka et al., 1999; Ishizuka et al., 2011).

3. Data and methods

Bathymetric data are extracted from the global grid, SRTM15_PLUS (Tozer et al., 2019). The seismic reflection profiles A-A' and B-B' were acquired in 2020 by the R/V "Dayanghao" from the Second Institute of Oceanology, Ministry of Natural Resources, China. The survey utilized an air gun array with a total volume of 6040 cubic inches, discharged at consistent intervals of 37.5 m while the vessel maintained a speed of approximately 5 knots. Seismic signals were captured using a 6-km-long streamer, equipped with 480 channels. The setup yielded a record length of 14 s, with data sampled every 2 ms.

The seismic data were processed through several steps to enhance quality and clarity. Noise reduction and signal enhancement were first achieved via filtering and deconvolution. Velocity analysis was then

conducted to determine the seismic wave speeds through different layers. Time migration was performed to correct the geometry of dipping reflectors and accurately position seismic events. Depth migration further transformed these time-aligned sections into depth profiles, offering a three-dimensional perspective of the subsurface.

Root Mean Square (RMS) velocities from time migration were converted into interval velocities using the Dix formula (Dix, 1955). This step is crucial for identifying variations in material densities and velocities, as materials at greater depths generally have higher densities and velocities. Interval velocity variations serve as key indicators of high-velocity anomalies, aiding in tracing the upward movement of denser materials, such as those forming oceanic core complexes.

Profile A-A' intersects the CBF at a 30° angle, leading to a systematic distortion in the observed dip angles due to its angled intersection with the fault planes. Correcting this obliquity to determine true dip values from apparent dips requires a trigonometric correction method. This method adjusts the apparent dip (δ_{app}) based on the profile's obliquity angle (θ) to the spreading axis.

The correction formula is given by:

$$\delta_{true} = \arctan\left(\frac{\tan\delta_{app}}{\cos\theta}\right)$$

where δ_{true} represents the true dip angle, δ_{app} is the apparent dip angle measured from the profile, and θ is the obliquity angle. The obliquity angle is defined as the acute angle between the profile direction and the true dip direction. In this study, the obliquity angle was determined to be 60°.

4. Seismic observations

The main seismic profile A-A' crosses three bathymetric highs: the southern ridge shoulder, a structural high within the rift valley, and the northern ridge shoulder (Fig. 2B). The structural high, situated between these two ridge shoulders, divides the profile into areas characterized by N-S and NE-SW rift valleys (Fig. 2B), reflecting the latest extensional reorientation (Fig. 3). Based on these observations, we have divided Profile A-A' into three segments: Segment ① across the southwest ridge flank of the WPB (Fig. 4); Segment ② across the latest NE-SW rift valley, bounded by the southern ridge shoulder and the structural high (Fig. 4); and Segment ③ across the N-S rift valley and the northern ridge shoulder (Fig. 5).

We present seismic reflection features from SW to NE, examining each segment in turn. We first propose a classification of the observed seismic reflectors, denoted by R1 – R18 in Table 1, and then describe the

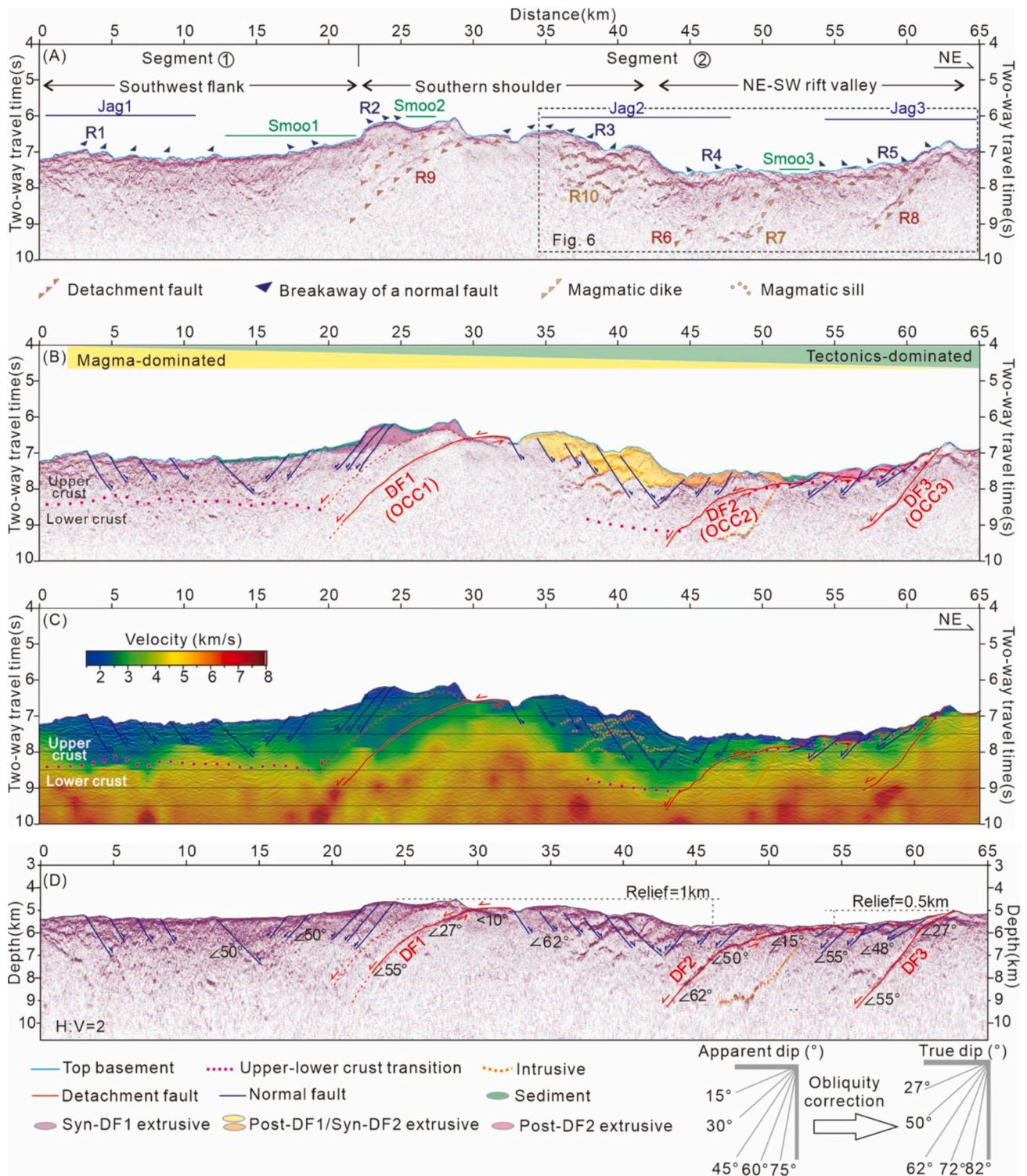


Fig. 4. Segments ① and ② of the MCS profile A-A', extending from the southwest ridge flank to the NE-SW rift valley of the basin. MCS image in the time domain (A) and its geological interpretation (B). (C) Superimposition of the MCS image and the interval velocity model along the profile. (D) Depth-migrated section with true dips of faults after a 60° obliquity correction. Segment ① exhibits a smooth top basement and uniform oceanic crust thickness, occasionally interrupted by high-angle normal faults (in blue), suggesting a magma-dominated spreading process. In contrast, segment ② features a rough top basement and detachment faults (DF1, DF2, and DF3 in red). High velocities in the footwalls of the detachment faults hint at an upwelling of deep materials linked to detachment faulting, indicating a highly tectonized oceanic crust. A dashed red line indicates a potential detachment fault parallel to DF1, while this study primarily focuses on the more robustly identified DFs1-3. Dotted pink lines mark the transition between the upper and lower crust. Refer to Section 6.2 for a discussion on *syn*- and post-detachment extrusions. (For interpretation of the references to colour in this figure legend, the reader is referred to the web version of this article.)

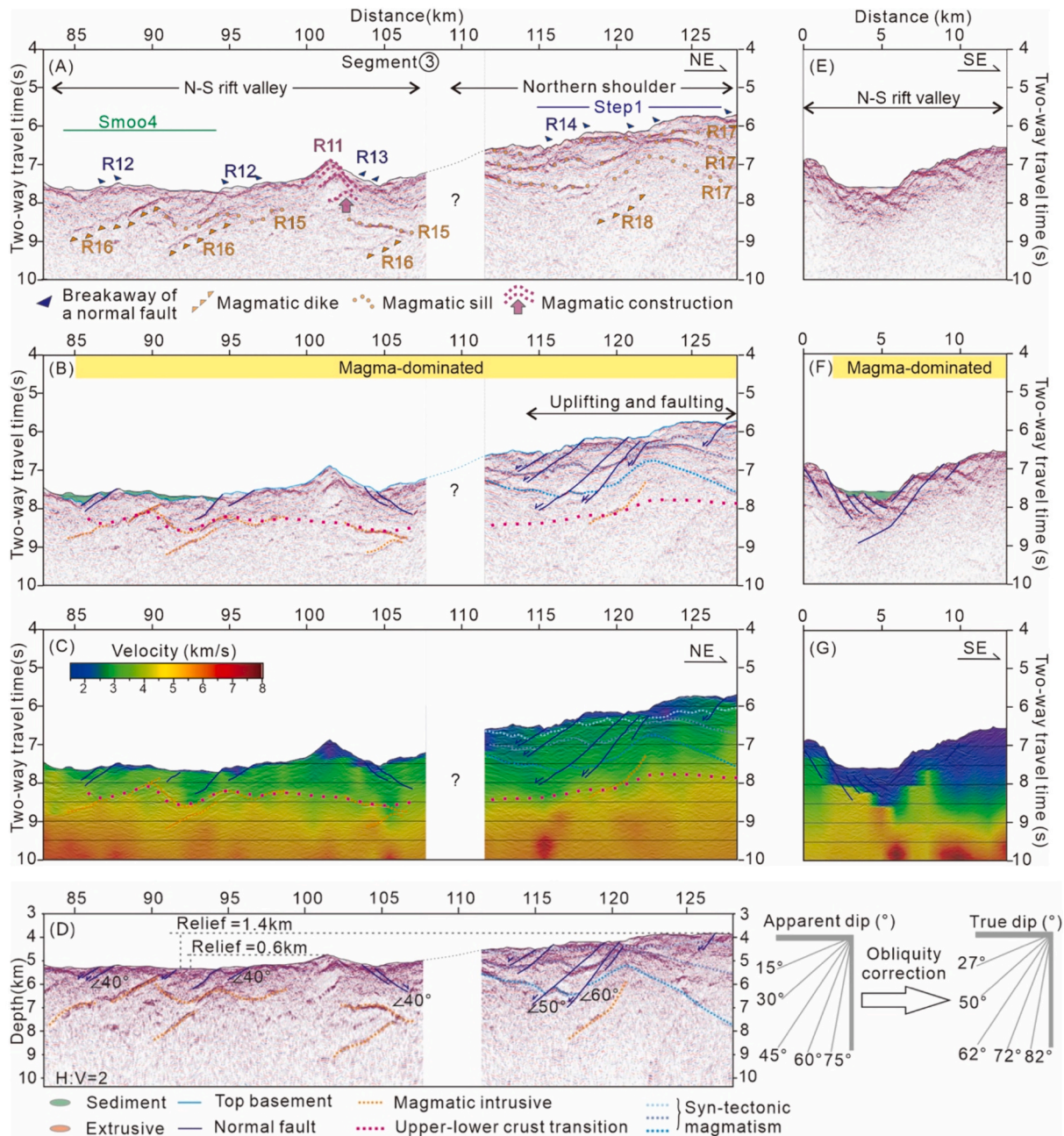


Fig. 5. Segment ③ of Profile A-A' (A-D) and Profile B-B' (E-G) crossing the eastern end of the CBF formed by N-S seafloor spreading. MCS image of Segment ③ in the time domain (A) and its geological interpretation (B). (C) Superposition of Segment ③ and its interval velocity model. (D) Depth-migrated section of Segment ③ with true dips of faults after a 60° obliquity correction. (E) Seismic profile B-B' perpendicular to profile A-A' and its geological interpretation (F). (G) Superposition of profile B-B' and its velocity model. Segment ③ and Profile B-B' reveal that the eastern end of CBF is characterized by thick extrusive layers in the upper crust, penetrated by high-angle normal faults with contrasting dips on either side of the valley, indicating magmatism dominated the N-S-oriented seafloor spreading.

characteristics of these reflection features in Section 4, followed by grouped interpretations in Section 5 (Figs. 4–5).

4.1. Segment ①: Southwest ridge flank

4.1.1. Top basement

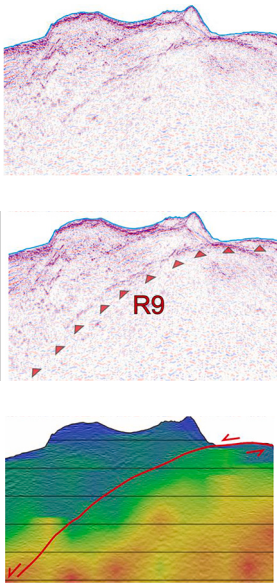
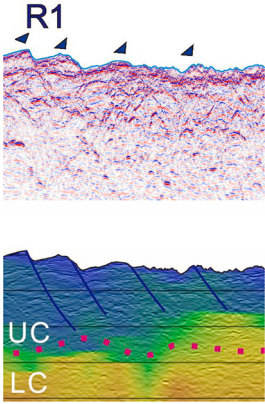
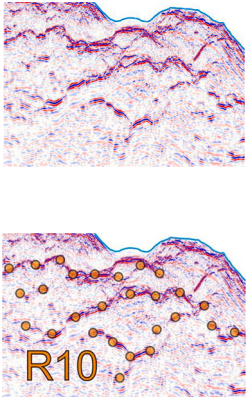
The seafloor in Segment ① is identified at depths between 6.5 and 7 s TWTT (4.8–5.2 km below sea level), featuring both smooth and jagged reflections (Fig. 4A). Smooth seafloor, at a distance of 12–22 km along the profile (marked as Smoo1 in Fig. 4A), bounds a thin sequence of parallel reflectors beneath (highlighted in green in Fig. 4B, detailed in Table 1) characterized by low interval P-wave velocities (<2.5 km/s,

Fig. 4C). Jagged seafloor (marked as Jag1 in Fig. 4A) is characterized by sub-horizontal reflectors interrupted by high-angle dipping reflectors (R1 and R2, Fig. 4A).

4.1.2. Intra basement

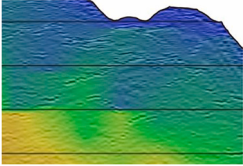
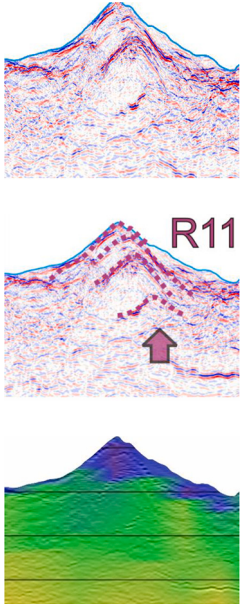
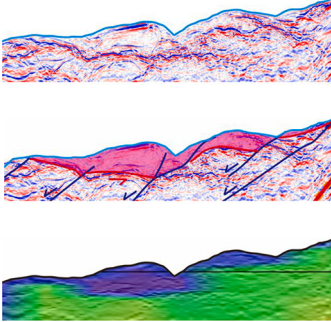
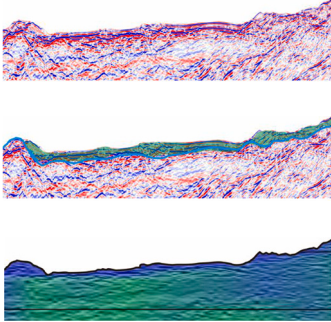
Beneath the top basement, the upper unit shows moderate-amplitude and disruptive reflectors in the MCS profile. This unit is frequently penetrated by high-angle dipping reflectors, R1 and R2, exhibiting low velocities (< 4 km/s, Figs. 4A–4C, detailed in Table 1). The NE-dipping reflectors at a distance of 0–15 km (R1) and the SW-dipping reflectors at a distance of 15–25 km (R2) form a symmetric structure (Figs. 4B–4C). The deepest penetration of reflectors R1 and R2 is observed at

Table 1
Groups of the seismic reflection features and their geological interpretations.

Group	Example	Reflection pattern	Velocity	Interpretation
R6, R8-R9		Moderate-amplitude, concave-down geometry with a large-scale surface expression (>10 km horizontal displacement) and penetrating deep crustal levels (> 9 km in depth)	High-velocity (> 5.5 km/s) at footwall	Detachment fault
R1-R5, R12-R14		High- to moderate-amplitude, sub-planar geometry, high-angle (>45°) dipping reflectors that offset the seafloor and terminate at the transition between the upper crust (UC) and the lower crust (LC)	Low velocity (< 4 km/s) at both hanging wall and footwall	High-angle normal fault
R7, R10, R15-R18		Sub-planar geometry or irregular shape, high-amplitude reflectors	No significant velocity anomaly	Magmatic sill or dike

(continued on next page)

Table 1 (continued)

Group	Example	Reflection pattern	Velocity	Interpretation
				
R11		High-amplitude, parallel reflectors showing a constructive structure	Low-velocity (< 4 km/s) within the structure	Volcanic edifice
Yellow, pink, and orange sequences in Segment ②		Bounded by high-amplitude reflectors with internal parallel, moderate- to low-amplitude reflectors	Extremely low-velocity (< 2.5 km/s)	Magmatic extrusive
Green sequence		Parallel, horizontal, and continuous reflectors beneath the smooth seafloor	Extremely low-velocity (< 2.5 km/s)	Sediment layer

approximately 8 s TWTT, marking a transition zone where amplitude changes from moderate to low (Figs. 4A-4B) and velocity increases from <4 km/s to >4.5 km/s (Fig. 4C). This transition is marked as dotted pink lines in Figs. 4B-4C.

4.2. Segment ②: NE-SW rift valley

4.2.1. Top basement

Segment ② features a rougher seafloor topography compared to Segment ①. The water depth increases from 6 s to 7.5 s TWTT over a distance of <15 km, from the southern ridge shoulder to the rift valley and forming a relief of 1 km (Fig. 4D). The seafloor is frequently interrupted by high-angle dipping reflectors (R3-R5, Fig. 4A), with R3 dipping parallel to the NE while R4 and R5 dipping to the SW (Fig. 4B). Beneath the seafloor, three sequences of low-amplitude reflectors can be observed, colored yellow, orange, and pink in Fig. 4B. Specifically, the yellow sequences incline slightly towards the SW, the orange sequences dip to the NE, and the pink sequences maintain a horizontal orientation (Fig. 4B, detailed in Fig. 6 and Table 1). These sequences thicken towards the high-angle dipping reflectors R3-R5 individually and exhibit low-velocity characteristics (<2.5 km/s in Fig. 4C, detailed in Fig. 6B).

4.2.2. Intra basement

Below the top basement, three sets of SW-dipping reflectors, R6, R7, and R8, are evident (Fig. 4A), all terminating at a depth of 9.5 s TWTT (Figs. 4A-4B). Specifically, R6 is characterized by continuous patterns with moderate amplitude, extending over a horizontal distance of 45–60 km and a depth range of 7.5–9.5 s TWTT. High velocities (>5.5 km/s) are observed alongside R6, from deep levels (9.5 s TWTT) up to near the surface (7.5 s TWTT) (Fig. 4C). After obliquity correction, the shallow part of R6 in the depth-migrated section shows a gentle angle at the surface, with true dips of $<15^\circ$, while its deepest part exhibits steep

true dips of 62° (Fig. 4D). Overall, R6 forms a concave-down geometry with a large-scale surface expression that encloses the high velocities (Figs. 4B-4D).

R7, observed at a depth of 8–9.5 s TWTT and at a distance of 45–50 km, mostly maintains a planar geometry and aligns parallelly to R6 (Fig. 4A), without notable features in its velocity structure (Fig. 4C). In contrast to R6, R7 shows a gentle angle at its deepest part and merges with R6 at a steep angle near the surface (Fig. 4D). These observations indicate a different geological origin compared to R6 (for a detailed discussion see Section 5.3).

R8 is characterized by its pronounced amplitude (Fig. 4A) and contrasting velocities on either side (Fig. 4C). Similar to R6, high velocities are distributed along R8, from a depth of >9.5 s TWTT to the shallow levels (Fig. 4C). However, R8 remains steeply inclined without showing a gentle surface angle as observed in R6 (for a detailed discussion see Section 5.1).

4.3. Segment ②: Southern ridge shoulder

4.3.1. Top basement

The seafloor at the southern ridge shoulder is characterized by high-amplitude reflectors (Fig. 4A). Specifically, on the SW side of the southern shoulder (a distance of 22–35 km), the seafloor is constituted by continuous and smooth reflectors (Smoo2, Fig. 4A). In contrast, the NE side of the southern shoulder (a distance of 35–45 km) displays a jagged seafloor (Jag2, Fig. 4A), and is interrupted by a series of high angle dipping reflectors (R3). These reflectors, dipping to the NE, penetrate to a depth of 2 s TWTT (Figs. 4A-4B).

4.3.2. Intra basement

Beneath the top basement, a concave-down geometry is evident at a distance of 22–35 km and a depth of 7–9 s TWTT (R9, Fig. 4A). The

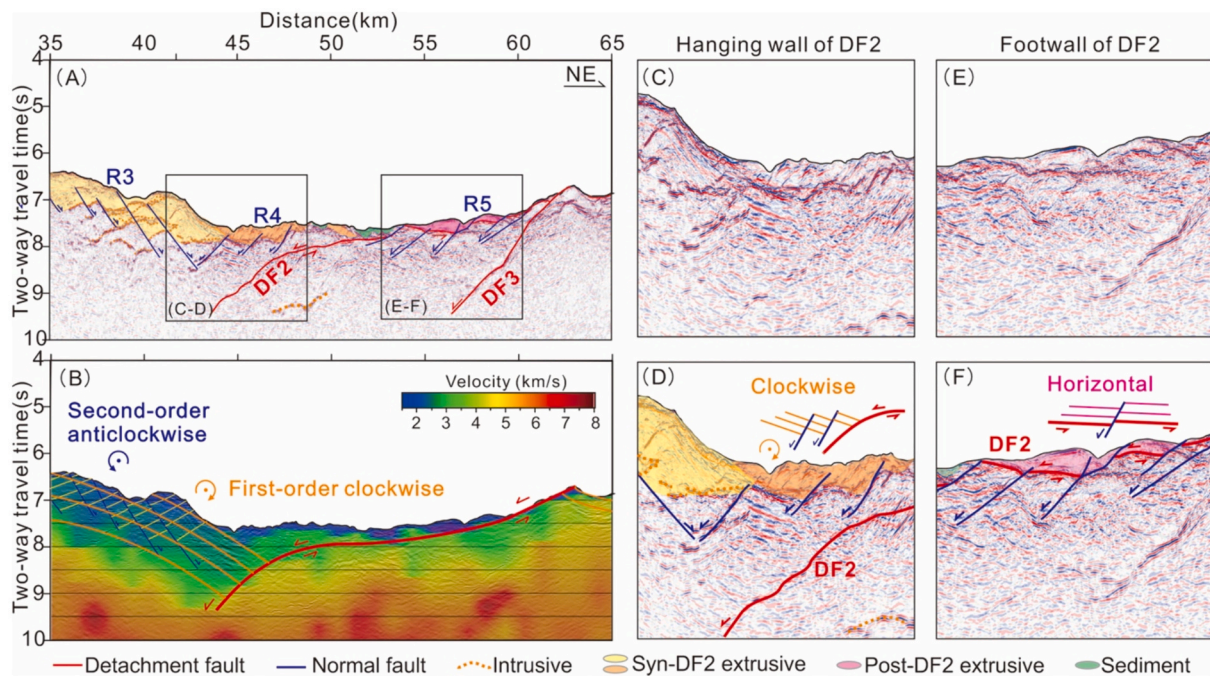


Fig. 6. Detailed view of the NE-SW rift valley within the WPB. (A) MCS image in the time domain and its geological interpretation. DF2 shows a concave-down geometry with large horizontal displacements (>15 km). (B) Interval velocity model for the detailed area and a simplified interpretation of the fault patterns. The top basement on the southern shoulder forms a rollover anticline (indicated by solid orange lines), suggesting a large-scale clockwise rotation under the slipping of DF2. Additionally, a series of NE-dipping normal faults (marked by solid blue lines) exhibit a smaller-scale anticlockwise rotation. (C–D) Zoom-in of the extrusive in the hanging wall of DF2. The observed clockwise rotation indicates that the yellow and orange extrusive sequences are synchronous to the slipping of DF2. (E–F) Zoom-in of the pink extrusive sequence in the footwall of DF2. Their internal reflectors show horizontal orientation, thickening towards the high-angle normal faults R5. This pattern suggests that these pink-colored extrusives are synchronous with high-angle normal faulting of R5 but post-date detachment DF2. (For interpretation of the references to colour in this figure legend, the reader is referred to the web version of this article.)

upper part of R9 reaches the seafloor at a distance of 30 km, while its lower part steeply dips to the SW, parallel to R6 - R8. Except for R9, the southern shoulder predominantly exhibits low-amplitude reflectors within the basement. Similar to R6 and R8 in the rift valley, high velocities (> 4.5 km/s) run along R9 from deep to shallow levels (Fig. 4C).

Northeast of the southern shoulder (a distance of 35–45 km), numerous high-amplitude, lateral-extending reflectors, R10, are observed at a depth of 6–8 s TWTT (Fig. 4A). The sequence where R10 occurs (colored by yellow in Fig. 4B and detailed in Fig. 6) is intersected by NE-dipping reflectors R3, corresponding to low velocities (< 3 km/s, Fig. 4C).

4.4. Segment ③: N-S rift valley

4.4.1. Top basement

In the N-S rift valley, an edifice featuring a relief of 500 m is marked by high-amplitude reflectors dipping away from its peak (R11, Fig. 5A). To the southwest of the edifice, the top basement is mostly smooth (Smoo4, Fig. 5A), occasionally interrupted by high-angle, SW-dipping reflectors (R12, Fig. 5A). A thin sequence of parallel reflectors is located at a distance of 85–95 km (green sequence, Fig. 5B). Northeast of the edifice, the top basement becomes shallower and is intersected by a series of NE-dipping reflectors (R13, Fig. 5A). At the northern ridge shoulder, the seafloor steps to the NE, shallowing from a depth of 6.5 s TWTT (4.8 km) to 5.5 s TWTT (4 km) (Step1, Fig. 5A).

4.4.2. Intra basement

Underneath R11, high-amplitude, moderate-continuous reflectors parallel to the surface form a constructive structure (Fig. 5A and detailed in Table 1). Reflectors R12 and R13 dip away from the edifice, penetrating 0.5 s TWTT below the top basement (Fig. 5A), within areas where velocities remain low (< 4 km/s, Fig. 5C). At the northern ridge shoulder, R14 penetrates deeper than 2 s TWTT below the top basement, intersecting three sets of high-amplitude, sub-horizontal reflectors (R17) at a depth of 6–7.5 s TWTT. The sequences bounded by the seafloor and R17 thicken towards R14 and exhibit a clockwise rotation. The distribution of R14 and R17 is within the upper unit, characterized by velocities < 4 km/s (Fig. 5C).

At a depth of 8–8.5 s TWTT, a series of sub-horizontal, moderate-amplitude reflectors displaying wavy patterns are observed (R15, Fig. 5A). Separated by R15, the lower unit exhibits lower amplitude reflections compared to the upper unit. Consistently, a notable increase in interval velocities (> 4.5 km/s, Fig. 5C) marks this transition, highlighted by dotted pink lines in Figs. 5B–5C. High-angle, SW-dipping reflectors, R16 and R18, are observed at a depth of 8.5–9.5 s TWTT, with R16 merging with the wavy reflectors of R15 at their shallowest parts (Fig. 5A). Neither R16 nor R18 show significant velocity anomalies (Fig. 5C).

5. Geological interpretations

5.1. Detachment faults

One of the most significant findings along Profile A-A' is that the reflectors R6, R8, and R9 extend over long horizontal distances (> 10 km) from depths > 9 km to the seafloor (Fig. 4). Specifically, R6 and R9 show steep dips exceeding 55° at their rooting zones, and progressively flatten as they approach the seafloor, forming a concave-down geometry in the depth section (Fig. 4D). High velocities are observed along R6 and R9, extending from deep levels to the surface (Fig. 4C). Based on the concave-down geometry and the high-velocity in the footwall, we interpret R6 and R9 as detachment faults, labeled DF2 and DF1 respectively, along with their associated OCCs (Fig. 4). Tectonic movements along DF1 and DF2 may be responsible for the exhumation of the lower crust and/or mantle materials, as indicated by the high velocities at the shallow surface, suggesting an ultra-thinned upper crust (detailed

discussions in Section 5.4).

Similarly, R8 encapsulates high velocities and maintains a parallel orientation with R6, suggesting the formation of another detachment fault along R8 (Fig. 4). However, DF3 displays a constantly steep dip without the typical concave-down geometry observed for DF1 and DF2. This steep inclination may indicate that DF3 is a detachment fault in an embryonic stage (detailed discussions in Section 6.1.2).

In addition to the three primary detachment faults (DFs1–3) that are the focus of this study, we have identified a potential fourth detachment fault in the hanging wall of DF1, dipping parallel to it. This structure is, however, less clearly defined in our data compared to DFs1–3. While shown in our interpretations (Fig. 4), it is not a central focus of our analysis due to the uncertainty in its identification.

Although our seismic acquisition system possessed the theoretical capability to detect the Moho, we did not observe clear evidence of a Moho reflector in the common mid-point gathers. This absence is attributed to the development of OCCs in the study area. OCCs are known to obscure Moho reflections through a combination of factors, including structural complexity, serpentinization processes, and the formation of gradational crust-mantle transitions. While a visible Moho would have provided valuable insights into the crustal thickness and magma supply, its absence is consistent with observations in analogous tectonic settings and offers indirect evidence of the significant crustal alterations associated with OCC formation.

These observations reveal that Profile A-A' features three sets of detachments: DF1, DF2, and DF3, each exhibiting a consistent SW-dipping orientation. DF1 is located on the southern ridge shoulder, DF2 is within the NE-SW rift valley, and DF3 is in a high structural position between the NE-SW and the N-S rift valleys (Figs. 2B and 4).

5.2. Normal faults

As detailed in Section 4.1, in the southwest ridge flank, a group of reflectors, labeled R1, shows a high-angle dipping geometry that offsets the top basement (Fig. 4A). Similar seismic reflection features are observed in R2 and R3 at the southern shoulder, R4–R5 and R12–R13 in the rift valleys, as well as R14 at the northern shoulder (Figs. 4A and 5A). These reflectors penetrate shallow levels not exceeding 1 s TWTT (< 1.5 km in depth) where velocities are below 4 km/s (Figs. 4C and 5C). We interpret these reflectors as high-angle normal faults (Table 1), which result in jagged (Jag1–Jag3, Fig. 4A) or step-shaped seafloor (Step1, Fig. 5A). Across the entire profile, these high-angle normal faults appear as three pairs of conjugate dipping directions, forming three hinge axes at distances of 15 km, 43 km (Fig. 4), and 107 km (Fig. 5), respectively. These observations are comparable with normal faults seismically imaged in the Central Atlantic (Reston et al., 2004; Reston and Ranero, 2011). Our interpretation extends their findings by identifying multiple conjugate fault systems across a broader area and revealing numerous smaller faults that indicate finer-scale structure.

5.3. Magmatism and sediments

Beneath the smooth seafloor (Smoo1–Smoo3 in Fig. 4A, Smoo4 in Fig. 5A), sequences characterized by parallel, horizontal, and continuous reflectors - referred to as green sequences - are observed (as detailed in Table 1). Integrated with their low-velocity features, these green sequences are interpreted as sediment layers with a thickness of < 100 m (Figs. 4–5).

Beneath the jagged seafloor (Jag2–Jag3 in Fig. 4A), other thin sequences are observed, referred to as yellow, orange, and pink sequences, respectively (Fig. 4B). These sequences are characterized by (1) boundaries marked by high-amplitude reflectors, (2) internal reflectors with moderate- to low-amplitude, and (3) extremely low velocities of < 2.5 km/s (Fig. 4 and detailed in Fig. 6). These characteristics identify them as magmatic extrusive sequences (Table 1). The surficial low-velocity layer ($V_p = 2–3$ km/s) is attributed to high-porosity pillows

and flows (Christeson et al., 1994) and potential alteration (e.g., hydration) related to detachment faulting in this area.

The internal reflectors of the orange and pink sequences show distinct differences: R4 in the orange sequence exhibits a slightly higher amplitude and a more compact arrangement (Figs. 6C–6D) compared to R5 within the pink sequence (Figs. 6E–6F). Such differences indicate that the orange and pink sequences, along with R4 and R5, respectively, likely originated during distinct chronological periods (detailed discussions in Section 6.2).

Within the yellow extrusive sequence, a set of reflectors, R10, presents high-amplitude and irregular patterns without significant velocity anomalies (Fig. 4 and detailed in Table 1). In addition, R10 is frequently intersected by high-angle normal faults (R3). These observations indicate that R10 consists of magmatic sills that developed synchronously with the high-angle normal fault R3 (Table 1). A similar intersection relationship between normal fault R14 and magmatic intrusives R17 is observed at the northern shoulder (Fig. 5), indicating that magmatism synchronous with tectonic faulting has resulted in a step-shaped seafloor that shallows towards the NE.

Within the basement of the NE-SW rift valley, while both R6 and R7 exhibit parallel SW-dipping orientations, their intricate structures lead to different geological interpretations. The concave-down geometry and the high velocities along R6 from the deep crust to the surface are reminiscent of a detachment fault (Table 1; see Discussion 5.1 for details). In contrast, the deepest part of R7 shows sub-horizontal reflectors, differing from the typical steeply dipping reflectors found in the rooting zone of a detachment fault, as illustrated in DF2 (Fig. 4D). In addition, compared to R6, R7 shows a lower amplitude and an absence of significant velocity changes on either side. Based on these observations, we interpret R7 as magmatic dikes within the lower crust (Fig. 4). In slow-spreading settings characterized by low magma supply, such reflections likely represent the cumulative effect of multiple intrusions rather than a single thick dike.

In the N-S rift valley, a localized, high-relief structure, identified as R11, with internal constructive formation, is observed at a distance of 101 km (Fig. 5). Its constructive structure is compatible with R11 representing a volcanic edifice related to successive eruption events (Table 1). Beneath the volcanic edifice, two sets of high-amplitude, sub-horizontal reflectors (R15, Fig. 5A) separate the upper unit with low velocities (<4 km/s) and lower unit with high velocities (>4.5 km/s). Considering this transition in velocity marks the transition between the upper and lower crust (detailed discussions in Section 5.4), R15 is interpreted as a magmatic sill extending along the crustal transition zone (Figs. 5A–5C). Interrupted by R15, R16 displays steep dips without any notable velocity anomalies and is, therefore, best interpreted as magmatic dikes (Fig. 5A, Table 1).

5.4. Upper and lower crust

Based on the seismic reflection pattern, velocity structure, and the depth of normal fault penetration, the basement along the profile can be divided into upper and lower units; the boundary is marked by dotted pink lines (Figs. 4–5). The upper unit is frequently penetrated by high-angle normal faults and predominantly displays high- to moderate-amplitude (Figs. 4A and 5A) and low velocities (<4 km/s, Figs. 4C and 5C). These features indicate the upper unit represents the upper crust, corresponding to the extrusive igneous layer of the oceanic crust. In contrast, the lower unit displays low-amplitude (Figs. 4A and 5A) and high velocities (>4.5 km/s, Figs. 4C and 5C), and only three sets of detachment faults can reach the lower unit (Fig. 4). We interpret the lower unit as the lower crust, corresponding to the intrusive igneous layer of the oceanic crust.

Notably, in Segment ②, the upper-lower crust transition approaches the surface at distances of 30 km, 50 km, and 65 km, respectively. This observation suggests that the upper crust in these areas is significantly thinned, or even absent, which aligns with the presence of detachment

faults DF1 and DF2. This condition results from the exhumation of the lower crust and/or mantle in their footwalls, as discussed in Section 5.1.

5.5. Along-strike segmentation

Segment ① is characterized by its smooth top basement and uniform amplitude in seismic reflection, suggesting homogeneity in the geological structures and compositions within the upper crust. High-angle normal faults intersect Segment ① and terminate at the upper-lower crust transition. Despite these interruptions, Segment ① maintains a consistent thickness throughout the upper crust, underscoring a relatively stable process during accretion. This uniformity in reflection amplitude, coupled with the structural features, suggests a sufficient magma supply during oceanic crust accretion, resulting in a magmatic-dominated top basement in Segment ① (Fig. 4).

In contrast, Segment ② is characterized by a rougher top basement, extensive distribution of large-offset detachment faults, and an ultra-thin or completely absent upper crust. These characteristics indicate a low magma supply during the formation of the oceanic crust, leading to a tectonic-dominated top basement where OCCs are prevalent (Fig. 4).

As discussed in Section 5.3, Segment ③ exhibits magmatism synchronous with tectonic faulting, which has resulted in a progressive thickening of the upper crust from the rift valley towards the northern shoulder (Fig. 5). Observations from Profile B-B' are consistent with these findings, revealing a series of high-angle normal faults with contrasting dip orientations on either side of the rift valley (Figs. 5E–5F). Such configuration suggests that similar to Segment ①, magmatism dominated the formation of the oceanic crust in Segment ③.

In summary, seismic observations and interpretations of Profile A-A' reveal a transition from a magmatically dominated oceanic crust, characterized by a smooth magmatic-dominated top basement, shallow-penetrating normal faults, and relatively uniform or progressively changing crustal thickness (Segments ① and ③), to a highly tectonized oceanic crust, which is distinguished by its rough tectonic top basement, the local absence of the upper crust, and the widespread presence of OCCs in Segment ② (further details in Section 6.4).

6. Implications

In this section, we delve deeper into (1) the evolution of the detachment faults, (2) the interplay between tectonic faulting and magmatism, and (3) variations in fault patterns and their implications for magma supply during seafloor spreading. Finally, we compare slow-spreading ridges formed in back-arc settings (e.g., WPB) with those in open oceans (e.g., MAR and SWIR).

6.1. Evolution of detachment faults

6.1.1. Relationship between detachment faults and normal faults

The NE side of the southern ridge shoulder is characterized by a large-scale anticline with clockwise rotation in the hanging wall of DF2 (Figs. 6B–6D). As such, DF2 represents a first-order fault that accommodates most of the plate divergence. At a distance of 32–42 km, an array of NE-dipping normal faults (R3, Fig. 4A and 6A) accompanied by yellow extrusive sequences (Figs. 4B and 6A) exhibits smaller-scale anticlockwise rotation of each panel (Fig. 6B). These faults may be classified as second-order faults, as they accommodate less strain but over a wider area.

These structural relationships suggest that the hanging wall of DF2 underwent a first-order clockwise rotation, contemporaneously compensated by second-order anticlockwise rotations along normal faults R3 (Fig. 6B). Such observations indicate that the secondary normal faults formed simultaneously with DF2, accommodating hanging wall deformation but having minimal impact on the primary oceanic crustal architecture in this tectonic-dominated segment.

In the footwall of DF2, a series of SW-dipping normal faults R5 offset

the exhumed footwall (Figs. 4A and 6F). Such observations indicate at least two stages of tectonic faulting during the latest NE-SW extension, which include an initial phase of detachment faulting followed by subsequent high-angle normal faulting. These distinct stages suggest a sequential evolution of fault systems in response to the strain distribution and magmatic activity.

In summary, the interplay between detachment faults and normal faults reveals a sequential process that shapes the oceanic crust. Detachment faults play a primary role, accommodating extension and facilitating the exhumation of deeper crustal and mantle rocks. Subsequently, normal faults further dissect and modify the exposed basement structure.

6.1.2. Sequential development of detachment faults

As described in Section 5.1, the profile reveals three sets of detachment faults (Fig. 4). Both DF1 and DF2 show distinctive structures with concave-down geometries. Notably, the footwall of DF1 is shallower than the footwall of DF2, as evidenced by the 1 km relief (Fig. 4D). As discussed in Section 6.1.1, the rotation of the DF2's hanging wall formed the northeast side of the southern shoulder, potentially contributing to the uplift of DF1's footwall. Thus, it can be inferred that the older detachment fault DF1 underwent rotational adjustments influenced by the evolution of its successor, DF2.

As for DF3, its steep dip suggests an early stage in the development of a detachment fault. This interpretation agrees with kinematic models for detachment fault systems, which propose that detachment faults initiate with steep inclinations ($\sim 65^\circ$) before rotating to shallower angles (Cannat et al., 1997; Choi and Buck, 2012; Lavier et al., 1999; MacLeod et al., 2009; Sandiford et al., 2021). In this study, the parallel relationship between normal faults R5 and DF3 (Fig. 4) indicates that DF3 may have developed from one of these normal faults after the formation of DF2. However, before DF3 could evolve into a mature detachment fault with a concave-down geometry, the extension stopped. For a detailed discussion, see Section 6.2.2.

In summary, the development of successive fault systems evolved through three distinct sets: DF1, DF2, and DF3 (Fig. 7), progressing from

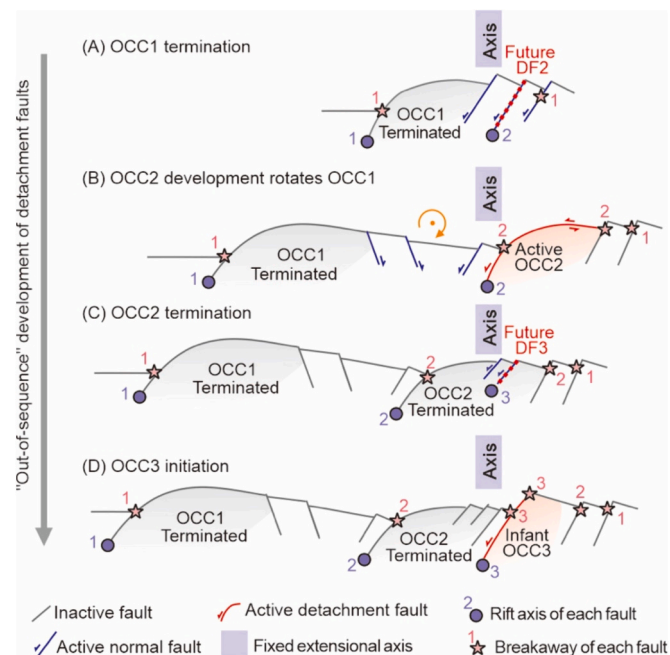


Fig. 7. Out-of-sequence development of detachment faults, with DF1 showing rotational adjustments influenced by DF2, while infant DF3 offsets DF2's exhumed footwall. All faults originate from a fixed deep rift axis but migrate outward, creating the appearance of shifting surface axes (1,2,3) while the deep initiation point remains stationary.

the southern ridge shoulder to the rift valley and the structural high. Their varying geometries—from fully developed concave-down (DF1 and DF2) to steep and embryonic (DF3)—reflect temporal and spatial variations in magmatic supply and tectonic activity.

While normal faults in the hanging wall resemble Reston and Ranero's (2011) rider block model, key differences exist. In the rider block model, new faults develop sequentially in the hanging wall of older faults. Gillard et al. (2016) introduced terminology to classify fault development patterns, referring to this sequential development as “in-sequence” faulting. However, our observations indicate a different pattern, which Gillard et al. (2016) termed “out-of-sequence” fault development, with younger faults appearing in older footwalls. Based on this contrasting pattern, we propose an out-of-sequence fault development model (Fig. 7), which is discussed further in Section 6.3.

6.2. Relationships between magmatic activity and faulting

6.2.1. Magmatism in the hanging wall of a detachment fault

As discussed in Section 5.3, the hanging wall of DF2 displays a first-order clockwise rotation, leading to the formation of yellow and orange extrusive sequences at a distance of 35–50 km and shaping the primary architecture of the oceanic crust (Figs. 4 and 6). Thus, we propose that the magmatic extrusion observed in the yellow and orange sequences occurred synchronously with DF2, referred to as *syn-DF2* extrusion.

Similarly, in the hanging wall of DF1, the internal reflectors within the extrusive sequence (marked in purple in Fig. 4B) dip towards DF1. This pattern indicates that the extrusion occurred simultaneously with detachment faulting, referred to as *syn-DF1* extrusion.

Within the yellow extrusive sequence, secondary normal faults R3 link to some of the magmatic sills R10 (Fig. 4A). This configuration could be interpreted as either faults acting as magma conduits or sills initiating fault formation. While the sill-initiated faulting model (Liu and Buck, 2022) effectively explains symmetric rift architecture at some mid-ocean ridges, it struggles to account for asymmetric rifts with large-offset detachment faults. We interpret pre-existing faults as preferential conduits for magma ascent and emplacement. This model better explains the observed synchronicity between magmatic intrusions and normal faulting (Fig. 6), as evidenced by the concurrent formation of the yellow extrusive sequence, normal faults R3, and detachment fault DF2.

6.2.2. Magmatism in the footwall of a detachment fault

In the footwall of DF2, the internal reflectors of the pink extrusive sequence (Figs. 4B and 6F) show a sub-horizontal reflection pattern (Fig. 6F) and thicken into the high-angle normal faults R5 (Fig. 6 and detailed in Table 1). From the kinematic analysis of a detachment fault evolution in Section 6.1.2, a detachment fault initiated with a high angle (Fig. 8A), then it evolved into a mature detachment fault with a low-angle surface (Fig. 8B). Subsequently, two potential scenarios can elucidate the timing of the pink extrusive sequences. In the first scenario, the extrusive sequence associated with the high-angle faulting emerges subsequent to the exhumation, forming a horizontal reflection pattern superimposed on the OCC (Fig. 8C). Conversely, the second scenario posits that magma extrusion occurs during the exhumation of the OCC. This synchronous occurrence would have resulted in the rotation of extrusive layers (reflections) (Fig. 8D).

Based on our analysis, the internal reflectors of pink extrusive sequences with a sub-horizontal pattern (Fig. 6F) align with the premises of scenario 1. Complementarily, insights from Section 6.1.2 elucidate that, the sequential development from detachment faulting of DF2 to high-angle normal faulting of R5 leads to the interpretation that normal faults function as conduits for magma migration and erupting on the exhumed footwall of DF2, forming the pink extrusive sequence (Fig. 8C). Consequently, we propose that this extrusion event materialized after the completion of the OCC development, a phenomenon we designate as *post-DF2* extrusion (Figs. 4, 6 and 8). This extrusive event effectively encapsulated the previously exhumed tectonic top basement (Fig. 8C).

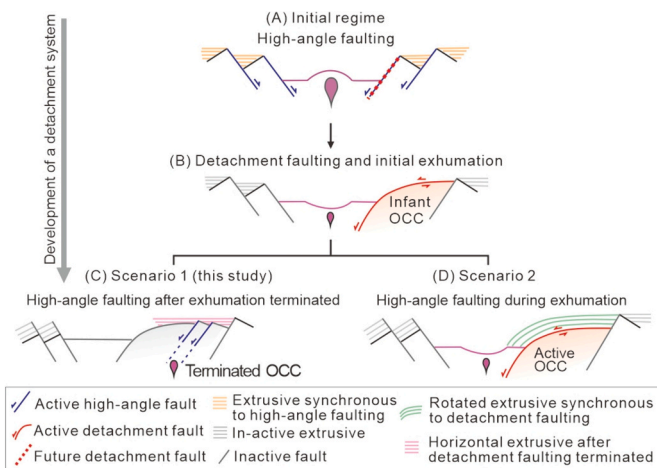


Fig. 8. Relationship between high-angle faulting, detachment faulting, and magmatic extrusion in detachment system development. (A) Symmetric high-angle normal faulting. (B) Rotation of a high-angle fault forms an early-stage detachment fault and infant OCC. (C–D) Two potential scenarios: (C) Magma extrusion associated with high-angle faulting after exhumation, forming a horizontal reflection pattern covering the OCC; (D) Extrusion and faulting during exhumation rotate extrusive layers. Observations from this study align with scenario 1.

This post-detachment extrusion has been proposed based on field observations in former oceanic domains exposed in the Alps (e.g., Coltat et al., 2020; Manatschal et al., 2023). Within the context of high-angle normal faulting, magma likely ascended via steep faults, subsequently settling atop the exhumed detachment fault. This would have eventually overwhelmed the development of the OCC, as suggested by Manatschal et al. (2011). Additional discourse on this topic can be found in Section 6.5. Our seismic interpretations support that the detachment faulting phase (or the prevalent OCC state) was superseded by a subsequent phase of syn-normal faulting magmatism, denoting the terminal phase of the OCC life cycle.

6.3. Evolution of a slow spreading system in the eastern WPB

Drawing from our discussions on sequential detachment faulting and magmatic activity, we present an evolution model for the slow seafloor spreading system in the eastern WPB (Fig. 9). Following Reston (2018), we distinguish between the “spreading axis” at the surface and the “rift axis” at depth, which denotes the divergence axis at fault initiation depth (Fig. 9).

6.3.1. Stage 1: high-angle faulting and magmatic accretion (Fig. 9A)

From 45 Ma to 33 Ma, seafloor spreading occurred with high magma supply, as observed in the southwest ridge flank (Segment ①, Fig. 4). According to the kinematic model by Deschamps et al. (2002), seafloor spreading at this period had an N-S orientation, producing uniform thickness crust with pronounced extrusive layers and shallow-penetrating normal faults (Fig. 9A). Thick extrusives and conjugate normal faults with contrasting dips (Segment ③ and profile B-B', Fig. 5) create a linear sharp spreading axis, marked as fixed extensional axis, accompanied by symmetric magmatic accretion (Fig. 9A). Subsequently, the extension orientation transitioned to NE-SW (Fig. 2, after Deschamps et al., 2002). As magma supply decreased, extension concentrated on one dominant high-angle normal fault, initiating DF1 at rift axis 1 (Fig. 9A).

6.3.2. Stage 2: detachment faulting and OCC development (Figs. 9B–9C)

DF1's rotation exhumed lower crust and mantle lithosphere, forming the mature OCC1 (Fig. 9B). Continued extension led to the development of DF2 closer to rift axis 2, exhuming deeper materials and forming

OCC2 (Fig. 9C). The younger DF2 developing on the footwall of the older DF1 indicates NE-ward migration of the rift axis (axis 2 in Fig. 9C).

6.3.3. Stage 3: high-angle faulting and post-exhumation magma extrusion (Figs. 9D–9F)

Following deep material exhumation, high-angle normal faults offset the top basement, providing pathways for magma extrusion (Fig. 9D). This post-OCC2 extrusion resulted in the observed pink extrusives covering OCC2 (Figs. 4B and 6F). Subsequently, a high-angle normal fault started to rotate, evolving into an early-stage detachment fault with steep angles (Fig. 9E), as observed in DF3 (Fig. 4D). Seafloor spreading ceased before OCC3 fully developed, preserving the infant detachment fault DF3 (Fig. 9E). As such, the final structure along profile A-A' was characterized by strong detachment faulting with local extrusives emplaced and covering the OCCs (Fig. 9F).

6.4. Fault patterns, magmatic supply, and tectono-magmatic interactions

The alternation between magmatic and tectonic top basements along profile A-A' suggests complex interactions between magmatic and tectonic activity in the eastern WPB. These interactions produce distinct crustal and top basement architectures and fault patterns reflecting variations in magmatic supply.

Magma-rich periods exhibit smooth top basements and shallow-penetrating high-angle faults (Segments ① and ③), indicative of pure-shear extension and symmetric patterns (Figs. 9A–9B, 10A and 10D). Conversely, magma-poor periods exhibit rough top basements, ultrathin or absent upper crust, and mantle exhumation at OCCs (Segment ②), suggesting simple-shear extension.

As magma supply decreases, fault displacement increases to compensate, leading to detachment faulting. This process results in the exhumation of the gabbroic lower crust and serpentinized mantle (Figs. 9C, 10B), localizing strain on active detachment faults and producing asymmetric structures.

Our model proposes a single, fixed deep rift axis as the extension point. Surface axes 1, 2, and 3 result from detachment faults propagating upward and outward from this fixed point. New faults initiate at the deep rift axis in young lithosphere but appear to form in older lithosphere as they migrate during plate spreading. This “rift axis” shifting mechanism is consistent with mechanical models (e.g., Buck, 1993; Lavier et al., 2000) and aligns with flipping detachments observed in the Southwest Indian Ridge (Reston, 2018; Sauter et al., 2013) and findings in Alpine analogs (Manatschal et al., 2011).

The dynamic nature of the system is further illustrated by the magmatic resurgence observed after the development of OCC2 (pink sequences in Figs. 4B, 6F, and 9E), terminating the detachment system DF2 and reestablishing symmetric, pure-shear extension. The apparent off-axis magmatism is a result of the outward migration of the rift axis over time.

In summary, our observations of the eastern WPB describe a transitional pattern, shifting from symmetric normal faults to asymmetric detachment faults and then back to symmetric normal faults (Figs. 9 and 10). This spatial variation in fault patterns correlates with changes in magma supply, suggesting a thermal structure evolving from magma-rich to magma-poor and then returns to magma-rich states.

6.5. Comparison of spreading between back-arc and mid-ocean ridge systems

In the back-arc, spreading center of the WPB, we observe three sets of detachment faults all dipping in the same directions (Fig. 10). This consistent dipping pattern is similar to that of the detachment faults at the MAR (Cannat et al., 1997; MacLeod et al., 2009), yet it contrasts with the varying dipping directions observed at the ultraslow SWIR (Sauter et al., 2013). The reasons behind the variability in dip direction within spreading systems are still unclear.

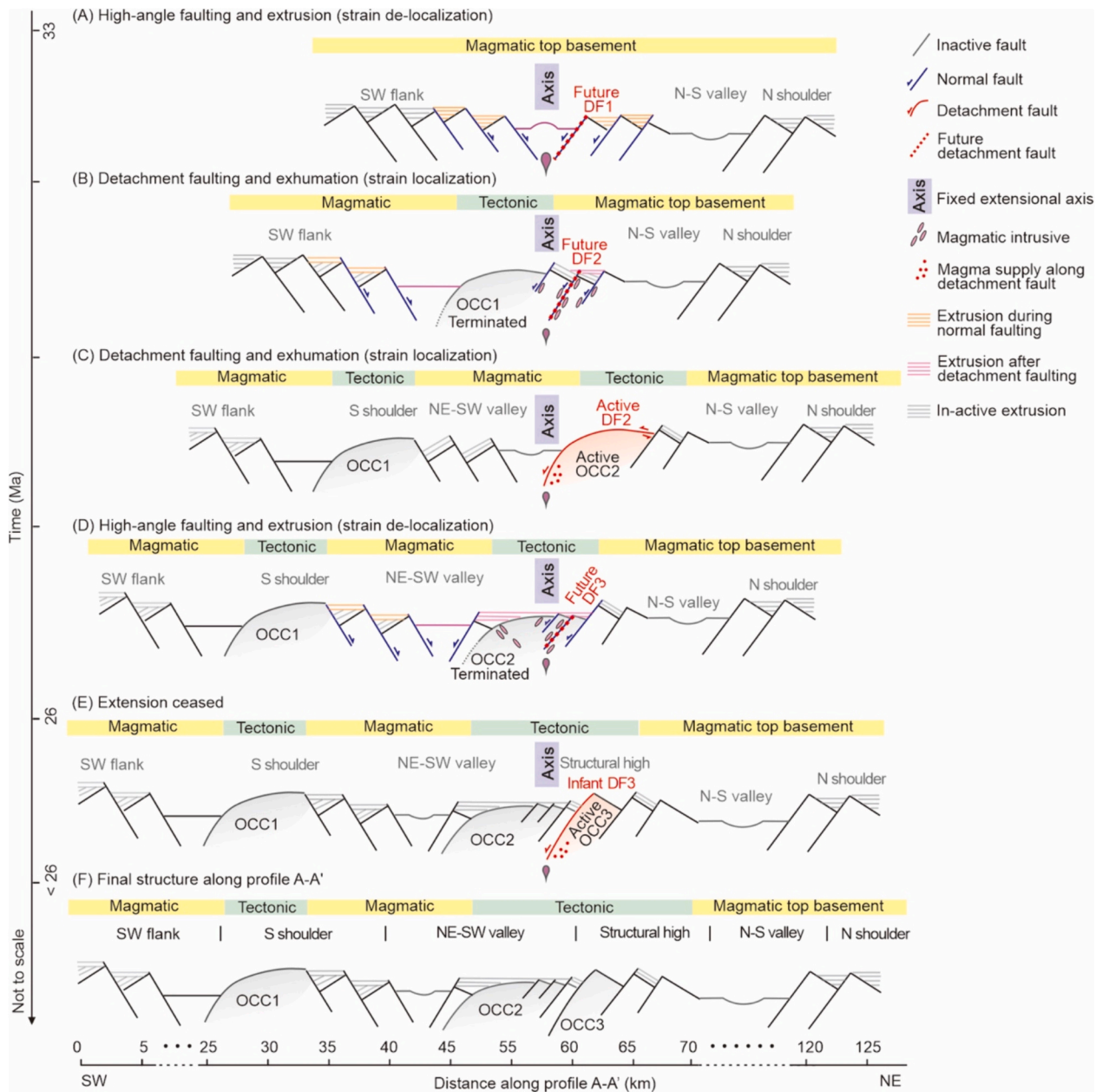


Fig. 9. Models illustrating the final stage of slow seafloor spreading in the WPB, showing the interaction between magmatism and tectonics over time. (A) Around 33 Ma, seafloor spreading shifted from high magma supply creating a magmatic top basement to decreased magma supply with dominant high-angle faulting. (B) A normal fault rotated into a mature detachment fault (DF1) and formed OCC1, creating a tectonic top basement. (C) Continued extension caused rotation in another fault, forming DF2 and OCC2, disrupting the magmatic top basement and indicating NE-ward migration of tectonic activity. (D) After OCC2's full exhumation, high-angle normal faults formed, creating conduits for magma and a thin extrusive layer, while DF3 began forming. (E) Seafloor spreading ceased before OCC3 fully developed, preserving the steep angles of infant DF3. (F) The final configuration alternates between magmatic and tectonic top basements as observed in the MCS profile A-A'. Time axis not to scale; refer to Section 2 for age descriptions.

Extrusives in the hanging wall of detachment faults commonly occur in slow-spreading systems, as observed in the volcanic zones at 26° N at the MAR (DeMartin et al., 2007). In the footwall of detachment faults, although extrusives overlying exhumed detachment faults have been reported, so far, the observations have been limited to sites where sections perpendicular to the former oceanic seafloor are exposed, for instance in the former oceanic domain exposed in the Alps (Coltat et al., 2020; Manatschal et al., 2023). Based on these geological outcrops, a conceptual model of an OCC life cycle has been proposed. It suggests that the rotation of the high-angle normal faults marks the initiation of a detachment system, and the increased magmatism eventually overwhelms and terminates its development (Manatschal et al., 2011).

Consistent with this model, our findings confirm not only the evolution of an OCC initiated by high-angle normal faulting, as demonstrated by the infant OCC3, but also the migration pathways of extrusives overlying exhumed detachment faults, as shown by the high-angle faults offsetting OCC2 (Figs. 8 and 9).

As proposed for slow and ultraslow MORs in open-ocean settings, seafloor spreading is usually characterized by: (1) separated large-scale detachment faulting that can be in- or out-of-sequence (e.g., MacLeod et al., 2009), (2) rider block formation where detachments develop in-sequence (e.g., Reston and Ranero, 2011), or (3) “flip-flop” detachment faults (e.g., Sauter et al., 2013). These different patterns are often associated with varying levels of magmatic budgets. Traditionally,

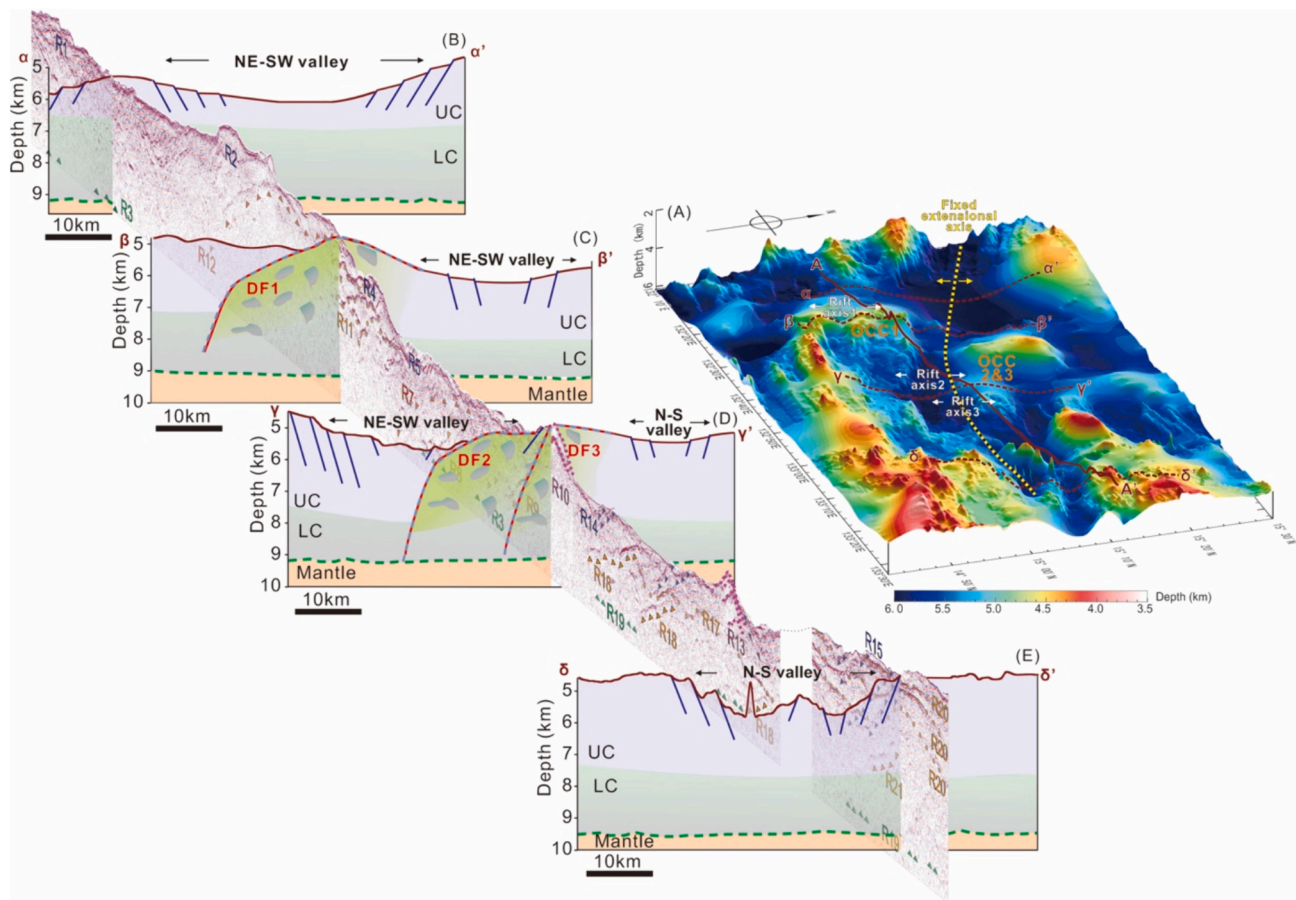


Fig. 10. 3D geological model (A) and geological interpretation of four cross-sections (B–E) perpendicular to the extensional axis based on profile A–A' (solid red line in A). The NE–SW extension features a wide, gently sloping valley flanked by OCCs, while the N–S extension presents a narrow, steep valley. Cross-sections β – β' and γ – γ' display three SW-dipping detachment faults (DFs1–3), indicating tectonic faulting with limited magma supply during NE–SW extension (C–D). Cross-section δ – δ' shows high-angle normal faults with opposing dips, uniform crustal thickness, and no OCC, suggesting a relatively high magma supply during N–S spreading (E). These findings indicate an along-strike variation in thermal-mechanical configuration. (For interpretation of the references to colour in this figure legend, the reader is referred to the web version of this article.)

variations in magmatic budget and changes from tectonic-dominated to magma-dominated spreading were thought to be primarily controlled by spreading rates (Buck et al., 2005; Liu and Buck, 2020; Sztikar et al., 2019; Tucholke et al., 2008). These models suggested a long-term relationship between plate motion and magma production.

However, recent studies suggested a short-term relationship between plate motion and magma production, i.e., melt supply (Cannat et al., 2019; Chen et al., 2022; Fan et al., 2021). Unlike spreading rates, which represent a long-term average, melt supply can vary on shorter time-scales and more locally, allowing for rapid shifts along strike (e.g., Escartín et al., 2008; Cannat et al., 2019).

In this study, we further demonstrate that the fault pattern and magma supply change simultaneously over a distance of ~ 70 km along strike. The close relationship between variations in melt supply and fault pattern indicates that along-strike strain distribution significantly influences melt generation and supply in this mid-ocean ridge setting. Areas of strain de-localization lead to increased decompression melting and higher melt supply, resulting in magmatic-dominated oceanic crust characterized by small-scale high-angle normal faults. Conversely, areas of strain localization result in reduced melting and lower melt supply, forming tectonic-dominated oceanic crust with detachment faults and exposure of serpentinized mantle. While this strain distribution plays a primary role in controlling melt generation and supply, it is important to note that the presence or absence of melt can also influence subsequent strain distribution, creating a feedback loop that contributes to the complex crustal architecture observed along the ridge. Our findings

provide a comprehensive framework for understanding how strain distribution plays a crucial role in influencing both magma supply and fault development, thus determining the fundamental character of the oceanic crust formed along different sections of the mid-ocean ridge.

7. Conclusions

Our investigation into the eastern MOR of the WPB has unveiled significant variations in fault patterns and magma supply, both across-ridge and along-strike of the ridge. We have documented a cycle of slow spreading that transitions from symmetric, magma-rich accretion to asymmetric, magma-poor spreading, ultimately leading to a stage where magmatism predominates, influencing the development of OCCs.

The interplay between high-angle normal faults and detachment faults highlights a transition from strain de-localization (pure-shear) to localization (simple-shear), which is closely linked to the variations in magma supply. This dynamic illustrates a shift from symmetric high-angle faulting associated with certain amounts of extrusive activity, resulting in a magmatic top basement, to the emergence of detachment faults with limited and localized extrusives, resulting in a tectonic top basement.

Our research has also brought to light both mature and infant OCCs within the basin, each representing different stages in the life cycle of detachment systems. Notably, the identification of an infant OCC in the axial valley underscores the potential for discovering more such formations with the aid of high-resolution seismic data, especially in

regions characterized by slow to ultra-slow spreading rates.

Our study advances this understanding by demonstrating a significant relationship between strain distribution, melt supply, and crustal characteristics over a distance of ~70 km along strike. Our findings reveal a strong link between tectonic processes and magmatic activity, where strain de-localization leads to increased melting and magmatic-dominated crust with high-angle normal faults, while strain localization results in reduced melting and tectonic-dominated crust featuring detachment faults and serpentinized mantle exposure. This comprehensive framework explains the observed variations in extension patterns and crustal structure along the ridge, bridging the gap between tectonic and magmatic processes in ridge evolution. By demonstrating how strain distribution simultaneously controls both magma supply and fault development, our study provides a new perspective for interpreting and predicting ridge morphology and behavior. These insights not only enhance our understanding of oceanic crust formation but also offer a more integrated view of the complex interplay between tectonic and magmatic processes at mid-ocean ridge settings.

Funding

This work was supported by the National Key Research and Development Program of China (2023YFF0803402), the National Natural Science Foundation of China (No. 42276082, No. 91858214, and No. 42025601), the Scientific Research Fund of the Second Institute of Oceanography, MNR (No. QNYC2301), and the Leading Talents in Scientific and Technological Innovation Project of Zhejiang Province (No. 2019R52034).

CRediT authorship contribution statement

Yanghui Zhao: Writing – review & editing, Writing – original draft, Visualization, Funding acquisition, Formal analysis, Data curation, Conceptualization. **Weiwei Ding:** Writing – review & editing, Supervision, Funding acquisition, Data curation. **Gianreto Manatschal:** Writing – review & editing, Visualization, Formal analysis. **Xiaodong Wei:** Methodology, Investigation, Formal analysis, Data curation. **Hanghang Ding:** Software, Data curation. **Zhengyi Tong:** Methodology, Data curation. **Jingyan Zhao:** Visualization, Formal analysis.

Declaration of competing interest

The authors declare that they have no known competing financial interests or personal relationships that could have appeared to influence the work reported in this paper.

Data availability

Bathymetric data are from (Tozer et al., 2019), available at https://topex.ucsd.edu/WWW_html/srtm15_plus.html. Uninterpreted MCS image datasets are available at doi:<https://doi.org/10.5281/zenodo.8437090>. Maps were constructed by using Generic Mapping Tools (GMT) version 6 (Wessel et al., 2019), available at <https://www.genericmapping-tools.org/>.

Acknowledgments

We thank Editor Claire A. Currie, reviewer Jean-Arthur Olive, and another anonymous reviewer for their comprehensive review and valuable feedback, which greatly enhanced this manuscript.

References

Arculus, R.J., Gurnis, M., Ishizuka, O., Reagan, M.K., Pearce, A., Sutherland, R., 2019. How to create new subduction zones: a global perspective. *Oceanography* 32, 160–174.

- Behn, M.D., Ito, G., 2008. Magmatic and tectonic extension at mid-ocean ridges: 1. Controls on fault characteristics. *Geochem. Geophys. Geosyst.* 9.
- Bell, R.E., Buck, W.R., 1992. Crustal control of ridge segmentation inferred from observations of the Reykjanes Ridge. *Nature* 357, 583–586.
- Buck, W.R., 1993. Effect of lithospheric thickness on the formation of high- and low-angle normal faults. *Geology* 21, 933–936. [https://doi.org/10.1130/0091-7613\(1993\)021<0933:EOLTOT>2.3.CO;2](https://doi.org/10.1130/0091-7613(1993)021<0933:EOLTOT>2.3.CO;2).
- Buck, W.R., Lavier, L.L., Poliakov, A.N.B., 2005. Modes of faulting at mid-ocean ridges. *Nature* 434, 719–723.
- Cann, J.R., Blackman, D.K., Smith, D.K., McAllister, E., Janssen, B., Mello, S., Avgerinos, E., Pascoe, A.R., Escartin, J., 1997. Corrugated slip surfaces formed at ridge-transform intersections on the Mid-Atlantic Ridge. *Nature* 385, 329–332.
- Cannat, M., Mével, C., Stakes, D., 1991. Stretching of the deep crust at the slow-spreading Southwest Indian Ridge. *Tectonophysics* 190, 73–94.
- Cannat, M., Lagabriele, Y., Bougault, H., Casey, J., de Coutures, N., Dmitriev, L., Fouquet, Y., 1997. Ultramafic and gabbroic exposures at the Mid-Atlantic Ridge: geological mapping in the 15 N region. *Tectonophysics* 279, 193–213.
- Cannat, M., Sauter, D., Mendel, V., Ruellan, E., Okino, K., Escartin, J., Combier, V., Baala, M., 2006. Modes of seafloor generation at a melt-poor ultraslow-spreading ridge. *Geology* 34, 605–608.
- Cannat, M., Sauter, D., Lavier, L., Bickert, M., Momoh, E., Leroy, S., 2019. On spreading modes and magma supply at slow and ultraslow mid-ocean ridges. *Earth Planet. Sci. Lett.* 519, 223–233. <https://doi.org/10.1016/j.epsl.2019.05.012>.
- Chen, Y., Morgan, W.J., 1990. Rift valley/no rift valley transition at mid-ocean ridges. *J. Geophys. Res.* Solid Earth 95, 17571–17581.
- Chen, J., Olive, J.-A., Cannat, M., 2022. Thermal regime of slow and ultraslow spreading ridges controlled by melt supply and modes of emplacement. *J. Geophys. Res.* Solid Earth 127, e2021JB023715. <https://doi.org/10.1029/2021JB023715>.
- Choi, E., Buck, W.R., 2012. Constraints on the strength of faults from the geometry of rider blocks in continental and oceanic core complexes. *J. Geophys. Res.* Solid Earth 117.
- Christeson, G.L., Purdy, G.M., Fryer, G.J., 1994. Seismic constraints on shallow crustal emplacement processes at the fast spreading East Pacific rise. *J. Geophys. Res.* 99. <https://doi.org/10.1029/94jb01252>.
- Coltat, R., Branquet, Y., Gautier, P., Boulvais, P., Manatschal, G., 2020. The nature of the interface between basalts and serpentinized mantle in oceanic domains: insights from a geological section in the Alps. *Tectonophysics* 797. <https://doi.org/10.1016/j.tecto.2020.228646>.
- DeMartin, B.J., Sohn, R.A., Canales, J.P., Humphris, S.E., 2007. Kinematics and geometry of active detachment faulting beneath the Trans-Atlantic Geotraverse (TAG) hydrothermal field on the Mid-Atlantic Ridge. *Geology* 35, 711–714.
- Deschamps, A., Lallemand, S., 2002. The West Philippine Basin: an eocene to early oligocene back arc basin opened between two opposed subduction zones. *J. Geophys. Res.* Solid Earth 107, EPM1-1-EPM1-24. doi:<https://doi.org/10.1029/2001jb001706>.
- Deschamps, A., Okino, K., Fujioka, K., 2002. Late amagmatic extension along the central and eastern segments of the West Philippine Basin fossil spreading axis. *Earth Planet. Sci. Lett.* 203, 277–293. [https://doi.org/10.1016/S0012-821X\(02\)00855-5](https://doi.org/10.1016/S0012-821X(02)00855-5).
- Ding, W., Zhu, R., Wan, B., Zhao, L., Niu, X., Zhao, P., Sun, B., Zhao, Y., 2023. Geodynamic processes of the southeastern Neo-Tethys Ocean and the formation mechanism of the curved subduction system in Southeast Asia. *Sci. China Earth Sci.* 66, 703–717.
- Dix, C.H., 1955. Seismic velocities from surface measurements. *Geophysics* 20, 68–86.
- Escartin, J., Smith, D.K., Cann, J., et al., 2008. Central role of detachment faults in accretion of slow-spreading oceanic lithosphere[J]. *Nature* 455 (7214), 790–794.
- Fan, Q., Olive, J., Cannat, M., 2021. Thermo-mechanical state of ultraslow-spreading ridges with a transient magma supply. *J. Geophys. Res.* Solid Earth 126, e2020JB020557.
- Fujioka, K., Okino, K., Kanamatsu, T., Ohara, Y., Ishizuka, O., Haraguchi, S., Ishii, T., 1999. Enigmatic extinct spreading center in the West Philippine backarc basin unveiled. *Geology* 27, 1135–1138.
- Gillard, M., Autin, J., Manatschal, G., 2016. Fault systems at hyper-extended rifted margins and embryonic oceanic crust: structural style, evolution and relation to magma. *Mar. Pet. Geol.* 76, 51–67. <https://doi.org/10.1016/j.marpetgeo.2016.05.013>.
- Hall, R., 2002. Cenozoic geological and plate tectonic evolution of SE Asia and the SW Pacific: computer-based reconstructions, model and animations. *J. Asian Earth Sci.* 20, 353–431.
- Hall, R., 2012. Late Jurassic-Cenozoic reconstructions of the Indonesian region and the Indian Ocean. *Tectonophysics* 570–571, 1–41. <https://doi.org/10.1016/j.tecto.2012.04.021>.
- Hansen, L.N., Cheadle, M.J., John, B.E., Swapp, S.M., Dick, H.J.B., Tucholke, B.E., Tivey, M.A., 2013. Mylonitic deformation at the Kane oceanic core complex: implications for the rheological behavior of oceanic detachment faults. *Geochem. Geophys. Geosyst.* 14, 3085–3108.
- Hilde, T.W.C., Lee, C.-S., 1984. Origin and evolution of the West Philippine Basin: a new interpretation. *Tectonophysics* 102, 85–104.
- Ishizuka, O., Taylor, R.N., Yuasa, M., Ohara, Y., 2011. Making and breaking an island arc: a new perspective from the Oligocene Kyushu-Palau arc, Philippine Sea. *Geochem. Geophys. Geosyst.* 12. <https://doi.org/10.1029/2010GC003440>.
- Ishizuka, O., Taylor, R.N., Ohara, Y., Yuasa, M., 2013. Upwelling, rifting, and age-progressive magmatism from the Oki-Daito mantle plume. *Geology* 41, 1011–1014. <https://doi.org/10.1130/G34525.1>.
- Lavier, L.L., Buck, W.R., Poliakov, A.N.B., 1999. Self-consistent rolling-hinge model for the evolution of large-offset low-angle normal faults. *Geology* 27, 1127–1130.

- Lavier, L.L., Buck, W.R., Poliakov, A.N.B., 2000. Factors controlling normal fault offset in an ideal brittle layer. *J. Geophys. Res. Solid Earth* 105, 23431–23442. <https://doi.org/10.1029/2000jb900108>.
- Lin, J., Purdy, G.M., Schouten, H., Sempere, J.-C., Zervas, C., 1990. Evidence from gravity data for focused magmatic accretion along the Mid-Atlantic Ridge. *Nature* 344, 627–632.
- Liu, Z., Buck, W.R., 2020. Global trends of axial relief and faulting at plate spreading centers imply discrete magmatic events. *J. Geophys. Res. Solid Earth* 125, 1–20. <https://doi.org/10.1029/2020JB019465>.
- Liu, Z., Buck, W.R., 2022. Magmatic sill formation during dike opening. *Geology* 50, 407–411. <https://doi.org/10.1130/G49400.1>.
- Louden, K.E., 1976. Magnetic anomalies in the West Philippine basin. *Geophys. Pac. Ocean Basin Margin* 19, 253–267.
- MacLeod, C.J., Escartin, J., Banerji, D., Banks, G.J., Gleeson, M., Irving, D.H.B., Lilly, R. M., McCaig, A.M., Niu, Y., Allerton, S., 2002. Direct geological evidence for oceanic detachment faulting: the Mid-Atlantic Ridge, 15° 45' N. *Geology* 30, 879–882.
- MacLeod, C.J., Searle, R.C., Murton, B.J., Casey, J.F., Mallows, C., Unsworth, S.C., Achenbach, K.L., Harris, M., 2009. Life cycle of oceanic core complexes. *Earth Planet. Sci. Lett.* 287, 333–344. <https://doi.org/10.1016/j.epsl.2009.08.016>.
- Manatschal, G., Sauter, D., Karpoff, A.M., Masini, E., Mohn, G., Lagabrielle, Y., 2011. The Chenaillet Ophiolite in the French/Italian Alps: an ancient analogue for an Oceanic Core complex? *Lithos* 124, 169–184. <https://doi.org/10.1016/j.lithos.2010.10.017>.
- Manatschal, G., Chenin, P., Ulrich, M., Petri, B., Morin, M., Ballay, M., 2023. Tectono-magmatic evolution during the extensional phase of a Wilson Cycle: a review of the Alpine Tethys case and implications for Atlantic-type margins. *Ital. J. Geosci.* 142, 5–27.
- Mrozowski, C.L., Lewis, S.D., Hayes, D.E., 1982. Complexities in the tectonic evolution of the West Philippine Basin. *Tectonophysics* 82, 1–24.
- Olive, J.-A., Behn, M.D., Tucholke, B.E., 2010. The structure of oceanic core complexes controlled by the depth distribution of magma emplacement. *Nat. Geosci.* 3, 491–495.
- Reston, T., 2018. Flipping detachments: the kinematics of ultraslow spreading ridges. *Earth Planet. Sci. Lett.* 503, 144–157. <https://doi.org/10.1016/j.epsl.2018.09.032>.
- Reston, T.J., McDermott, K.G., 2011. Successive detachment faults and mantle unroofing at magma-poor rifted margins. *Geology* 39, 1071–1074. <https://doi.org/10.1130/G32428.1>.
- Reston, T.J., Ranero, C.R., 2011. The 3-D geometry of detachment faulting at mid-ocean ridges. *Geochemistry. Geophys. Geosyst.* 12, 1–19. <https://doi.org/10.1029/2011GC003666>.
- Reston, T.J., Ranero, C.R., Ruoff, O., Perez-Gussinye, M., Dañobeitia, J.J., 2004. Geometry of extensional faults developed at slow-spreading centres from pre-stack depth migration of seismic reflection data in the Central Atlantic (Canary Basin). *Geophys. J. Int.* 159, 591–606. <https://doi.org/10.1111/j.1365-246X.2004.02444.x>.
- Sandiford, D., Brune, S., Glerum, A., Naliboff, J., Whittaker, J.M., 2021. Kinematics of footwall exhumation at oceanic detachment faults: solid-block rotation and apparent unbending. *Geochem. Geophys. Geosyst.* 22, 1–12. <https://doi.org/10.1029/2021GC009681>.
- Sauter, D., Cannat, M., Rouméjon, S., Andreani, M., Birot, D., Bronner, A., Brunelli, D., Carlut, J., Delacour, A., Guyader, V., MacLeod, C.J., Manatschal, G., Mendel, V., Ménez, B., Pasini, V., Ruellan, E., Searle, R., 2013. Continuous exhumation of mantle-derived rocks at the Southwest Indian Ridge for 11 million years. *Nat. Geosci.* 6, 314–320. <https://doi.org/10.1038/ngeo1771>.
- Schroeder, T., John, B.E., 2004. Strain localization on an oceanic detachment fault system, Atlantis Massif, 30° N, Mid-Atlantic Ridge. *Geochem. Geophys. Geosyst.* 5.
- Szitkar, F., Dymment, J., Petersen, S., Bialas, J., Klischies, M., Graber, S., Klaeschen, D., Yeo, I., Murton, B.J., 2019. Detachment tectonics at Mid-Atlantic Ridge 26° N. *Sci. Rep.* 9, 1–8. <https://doi.org/10.1038/s41598-019-47974-z>.
- Taylor, B., Goodliffe, A.M., 2004. The West Philippine basin and the initiation of subduction, revisited. *Geophys. Res. Lett.* 31.
- Tozer, B., Sandwell, D.T., Smith, W.H.F., Olson, C., Beale, J.R., Wessel, P., 2019. Global bathymetry and topography at 15 arc sec: SRTM15+. *Earth Sp. Sci.* 6, 1847–1864. <https://doi.org/10.1029/2019EA000658>.
- Tucholke, B.E., Behn, M.D., Buck, W.R., Lin, J., 2008. Role of melt supply in oceanic detachment faulting and formation of megamullions. *Geology* 36, 455–458. <https://doi.org/10.1130/G24639A.1>.
- Wessel, P., Luis, J.F., Uieda, L., Scharroo, R., Wobbe, F., Smith, W.H.F., Tian, D., 2019. The generic mapping tools version 6. *Geochem. Geophys. Geosyst.* 20, 5556–5564. <https://doi.org/10.1029/2019GC008515>.
- Zhang, M., Di, H., Xu, M., Canales, J.P., Yu, C., Zhao, X., Wang, P., Zeng, X., Wang, Y., 2022a. Seismic imaging of Dante's Domes oceanic core complex from streamer waveform inversion and reverse time migration. *J. Geophys. Res. Solid Earth* 127, e2021JB023814.
- Zhang, Z., Dong, D., Sun, W., Zhang, G., 2022b. Oligocene magmatic accretion and transtensional tectonics in the Central Basin Fault rift of the West Philippine back-arc basin: new insights from high-resolution multichannel seismic data. *Mar. Pet. Geol.* 141, 105703. <https://doi.org/10.1016/j.marpetgeo.2022.105703>.